THE ASTRONOMICAL JOURNAL VOLUME 114, NUMBER 3 SEPTEMBER 1997

THE NGC 281 WEST CLUSTER. I. STAR FORMATION IN PHOTOEVAPORATING CLUMPS

S. T. MEGEATH

MIT Haystack Observatory, Off Route 40, Westford, Massachusetts 01886-1299; and Max-Planck-Institut für Radioastronomie, Auf dem Hügel 69, D-53121 Bonn, Germany
Electronic mail: megeath@card.haystack.edn

T. L. WILSON

Max-Planck-Institut für Radioastronomie, Auf dem Hügel 69, D-53121 Bonn, Germany
Electronic mail: p073twi@mpifr-bonn.mpg.de

Received 1996 November 12; revised 1997 June 13

ABSTRACT

The NGC 281 West molecular cloud is an excellent test case for studying star formation in the clumpy interface between a H II region and a giant molecular cloud. We present here a study based on new high resolution radio and near-infrared data. Using the IRAM 30-meter telescope, we have mapped the interface in the $C^{18}O$ $(2\rightarrow1)$, $C^{18}O$ $(1\rightarrow0)$, and $C^{34}S$ $(3\rightarrow2)$ transitions with FWHP beamwidths $\leqslant 22''$. We have imaged the same region with the VLA in the 20, 6, and 2 cm continuum bands to obtain complementary maps of the ionized gas distribution with angular resolutions $\leqslant 13''$. In addition, we have obtained near-infrared J and K'-band images to detect young stars in the interface. The 30-meter data shows the molecular gas is concentrated into three clumps with masses of 570, >210, and 300 $M_\odot$ and average volume densities of 1.4, >1, and 2×10^4 cm^{-3}. We detect $C^{34}S$ $(3\rightarrow2)$ emission in two of the clumps, indicating peak densities in excess of 5×10^5 cm^{-3} are attained in the clumps. A comparison of the $C^{18}O$ line data with the 20 cm continuum image suggests that the molecular clumps are being photoevaporated through their direct exposure to the UV radiation from neighboring OB stars. The luminosity and extent of the observed 20 cm emission is in good agreement with models of photoevaporative flows. We use these models to estimate the pressure exerted on the clumps by the ionized gas and find that it exceeds the internal, turbulent pressure of the clumps by a factor of a 2.5. Although a pressure equilibrium is not excluded given the uncertainties inherent in determining the pressures of the ionized and molecular gases, our best estimates of the clump and flow parameters favor the existence of low velocity shocks (1.5 km s^{-1}) in the clumps. The clumps exhibit broad, non-Gaussian line shapes and complex kinematical structures suggestive of shocks. Further evidence for shocks is found in a comparison of position-velocity diagrams with published numerical simulations of imploding spherical clumps. We discuss the possibility that the knots of $C^{34}S$ $(3\rightarrow2)$ emission trace gas compressed by converging shock waves. The K'-band observations show a rich cluster of primarily low mass stars in the H II/molecular interface, which we argue is divided into two distinct sub-clusters. We associate one sub-cluster with the two clumps nearest the OB stars, and the second sub-cluster with the third clump. The two clumps nearest the OB stars contain an embedded stellar population, suggesting that star formation is ongoing. We discuss the impact photoevaporation is having on star formation in these two clumps. We find that photoevaporation is dispersing the molecular gas from which the cluster is forming and estimate that the molecular gas will be completely evaporated in 2.5 Myr. Deep K'-band imaging of the two clumps show that the stars are detected primarily on the sides of the clumps facing the OB stars and in the adjoining H II region. We examine three explanations for this asymmetry: the acceleration of the molecular clumps away from the stars by photoevaporation (i.e., the rocket effect), the unveiling of young embedded stars by ionization-shock fronts, and the triggered formation of stars by shocks advancing into the clumps. If shocks do indeed exist in the clumps, then we argue that shock triggered star formation is the best explanation of the asymmetry. © *1997 American Astronomical Society.* [S0004-6256(97)02909-9]

1. INTRODUCTION

UV radiation and stellar winds from young OB stars have a profound effect on the structure and evolution of molecular clouds and may play an important role in regulating star formation in galaxies. By ionizing the surrounding molecular gas, associations of OB stars photoevaporate the molecular clouds from which they form and ultimately destroy giant molecular clouds (GMCs) on a time scale of 10 Myr (Leisawitz, *et al.* 1989). However, before the clouds are destroyed, shocks driven into molecular clouds by the hot, photoionized gas may trigger the formation of new generations

 0004-6256/97/114(3)/1106/15/$10.00

of stars (Elmegreen 1992). The possibility of shock triggered star formation has received substantial attention from theorist and observationalist alike; however, despite the interest, observational evidence for various proposed triggering scenarios remains circumstantial and inconclusive.

The photoionization of a GMC and the subsequent propagation of shocks into the cloud can be significantly affected by the clumpy, inhomogeneous structure of the molecular gas. While low density gas is quickly ionized or swept away in shocks, high density clumps will impede advancing ionization-shock fronts. As the surrounding lower density material is dispersed, the clumps will emerge into the neighboring H II region. Lower density molecular gas in the shadow of a clump will be shielded from the direct ionizing UV radiation, and the molecular cloud may take on a cometary morphology with the dense clump forming the head of the comet. Once the clumps are fully exposed to the UV field of nearby OB stars; the surfaces of the clumps will be ionized. The expansion of the dense, ionized gas at the clump surface into the lower density H II region will result in a continual flow of mass off the clump; this process is referred to as photoevaporation.

Bright rimmed and cometary globules apparent in optical images of H II regions are thought to be examples of molecular clumps emerging into H II regions (Reipurth 1983). Recent numerical models of spherical clumps suddenly exposed to intense UV radiation have been successful at reproducing the morphologies of the observed globules (Lefloch & Lazareff 1994, hereafter LL94; Bertoldi & McKee 1990). Theoretical analyses show that in many cases, a converging shock wave will be driven into the clump (Bertoldi 1989, hereafter B89; LL94). The models predict that the compression of the molecular gas by the shock wave will eventually result in a cometary-shaped globule in pressure equilibrium with the surrounding photoevaporating gas. Furthermore, the globule will be accelerated away from the UV source as it photoevaporates. Evidence for such shocks and the resulting acceleration has been found in molecular line observations of cometary and bright rimmed globules (Patel *et al.* 1993; Patel *et al.* 1995; Megeath *et al.* 1996).

IRAS sources with colors characteristic of young stars have been found in numerous bright rimmed globules (Sugitanni *et al.* 1991; Sugitanni & Ogura 1994; Megeath *et al.* 1996). It is currently not clear whether the formation of these young stars has been triggered. In support of triggered star formation, Sugitanni *et al.* (1991) and Sugitanni & Ogura (1994) found that the average luminosity of *IRAS* sources in bright rimmed globules is significantly higher than the average luminosity of those in isolated globules with similar masses, suggesting that the star formation efficiency is enhanced in the bright rimmed globules. Furthermore, recent near-infrared (NIR) imaging has revealed that the young stars are concentrated near the photoevaporating edges of the globules (Sugitanni *et al.* 1995; Megeath *et al.* 1996). This configuration is suggestive of star formation triggered by ongoing shock compression. Nevertheless, detailed data on the internal structure and kinematics of bright rimmed globules are needed to confirm claims of triggered star formation. One such attempt was a study of a bright rimmed globule in IC 1396 by Serabyn *et al.* (1993). They concluded that photoevaporation has not significantly affected the globule's internal density structure, and consequently, they found it unlikely that the formation of the *IRAS* source in the globule had been triggered. Similar millimeter wavelength studies of a larger sample of globules are needed to reconcile claims for and against triggered star formation in bright rimmed globules.

The triggered formation of stars through the compression of pre-existing clumps is an alternative to the sequential star formation model proposed by Elmegreen & Lada (1977). In the Elmegreen & Lada model, an expanding H II region sweeps up low density molecular gas into a dense layer. Eventually, the high density layer becomes gravitationally unstable. The ensuing collapse and fragmentation of the layer may result in the formation of a cluster of stars. Elmegreen (1992) refers to this scenario as the "collect and collapse scenario." For comparison, triggered star formation in bright rimmed clouds must occur on much smaller size scales (1.0 pc) and time scales (0.5 Myr) than the size scales (10.0 pc) and time scales (1.0 Myr) implied by the Elmegreen & Lada scenario.

Given the important role photoionization may play in regulating star formation in molecular clouds, it is of great value to study in detail the propagation of an ionization front into a clumpy molecular cloud and its effect on star formation. We have recently investigated the H II/molecular interface of the NGC 281 West molecular cloud. The NGC 281 West molecular cloud has long been considered a potential site for triggered star formation (Elmegreen & Lada 1978; Henning *et al.* 1994). To study in detail the interaction of the H II region with the molecular cloud, we have obtained 13″ resolution VLA 20 centimeter images of the ionized gas component and 11″–22″ resolution IRAM 30-meter telescope observations of the molecular gas component. These observations are complemented by deep near-infrared imaging which provide a census of the population of stars in the H II region/molecular cloud interface.

1.1 The NGC 281 West Region

The NGC 281 West cloud is a moderately massive ($\sim$17000 $M_\odot$) outer galaxy molecular cloud at a heliocentric distance of 2.94 kpc (Henning *et al.* 1994; Guetter & Turner 1996). The molecular cloud obscures the southwestern quadrant of the nebulosity NGC 281 (also known as Sharpless 184), which is ionized by a small group of OB stars. The brightest member of the OB group is the trapezium system HD 5005, which provides most of the UV flux in the H II region. In Fig. 1 (Plate 58), we show a CCD image of the NGC 281 region taken in a narrow-band filter covering the Hα and [N II] lines. Superimposed is the ^{13}CO (1$\rightarrow$0) map from Carpenter *et al.* (1990).

The ^{13}CO (1$\rightarrow$0) emission peaks at the northern edge of the cloud near the H II/molecular interface (Fig. 1). A map in the CS (2$\rightarrow$1) line by Carpenter *et al.* (1993) shows a 210 $M_\odot$ molecular core coincident with the peak. Bright Hα emission is apparent near the H II/molecular interface, indicating that the cloud is interacting with the H II region. The ^{13}CO (1$\rightarrow$0) peak coincides with a luminous *IRAS* source

and is the only confirmed site of star formation in the NGC 281 West cloud. Coincident with this peak, Elmegreen & Lada detected an H_2O maser, Snell *et al.* (1990) found evidence for an outflow, and Carpenter *et al.* (1993), Hodapp (1994), and Megeath (1994) detected a cluster of low mass stars. Based on the proximity of the ^{13}CO $(1\rightarrow0)$ peak to the H II region and the evidence for ongoing star forming in the peak, Elmegreen & Lada (1978) suggested that NGC 281 west is a site of shock triggered star formation through a "collect and collapse" mode. Elmegreen & Moran (1979) provided some evidence for a shock using 2.3′ resolution ^{13}CO $(1\rightarrow0)$ and ^{12}CO $(1\rightarrow0)$ data.

The existing literature and the data presented in this paper show that NGC 281 West is an excellent laboratory for studying the effects of photoionization on molecular clouds and star formation. Although the study of this region is complicated by its large heliocentric distance (2.9 kpc), NGC 281 has several advantages over closer regions. First, there appears to be a clean separation between the ionized gas and the dense molecular gas on the rim of the H II region. Additionally, there are no known compact H II regions in the molecular cloud; hence, we can associate the observed ionized gas with the giant H II region. Finally, since NGC 281 (G123.1-6.3) is in the outer galaxy and out of the galactic plane, we find that the contamination of the near-infrared data by field stars is negligible. In total, these advantages make the study of this region a valuable complement to studies of closer regions such as Orion.

2. OBSERVATIONS AND DATA REDUCTION

2.1 Near-Infrared Data

We initially detected the cluster in 1991 September with the Prime Focus IR (PFIR) camera on the Palomar 5 m telescope.[1] During this observing session, we obtained the J-band data presented in this paper. At this time, the PFIR incorporated a 128×128 NICMOS2 chip with a 0.″78 pixel scale. We mapped the cluster taking care that each position was covered in 9 overlapping frames. The weather was photometric throughout the night. In 1991 November, we obtained K'-band data with a NICMOS3 camera on the University of Hawaii 2.2 meter telescope. During a period of light cirrus, we mapped a 4.′5 × 4.′0 region in the K' band (Wainscoat & Cowie 1992). The total integration time per pixel was 90 seconds. On subsequent nights, we obtained deep, photometric K' data of a 2.′1×2.′3 section of the cluster. The on-source integration time was 1500 seconds. Frames were also taken of a reference field 5′ east of the cluster to provide a field of "empty" sky with a sensitivity and spatial extent equivalent to the cluster data.

To reduce the J-band data, we subtracted a dark frame with an equivalent exposure time and then flat fielded the data. The flat field was created through median filtering the stack of dark frame subtracted reference field frames. The K'-band images were initially divided by a dome flat: the difference of frames taken of the dome with illuminating tungsten lights on and off. We then subtracted a sky frame created from the median of three sky frames taken immediately before and three sky frames taken immediately after the on-source frame. The K' and J-band images were registered using bright stars common to all images, and mosaicked using a Fortran program linked to IRAF. All noisy, nonresponsive, or nonlinear pixels were masked out.

The resulting point spread functions have FWHMs of 0.83″, 0.95″, and 1.26″ for the K' wide field, K' deep, and J-band data, respectively. The fainter stars in the displayed images are 21 (J), 18.5 (deep K'), and 17 (wide K'). By adding artificial stars to the deep K'-band data, we estimate that the deep K' image is 80% complete to 18.5 mag in non-confused areas of the image, but only 40% complete in the inner cluster due to confusion with brighter cluster members (Megeath & Herter 1997). To register the mosaics accurately, we obtained coordinates of bright, optically visible stars in the field by measuring their positions on the Palomar sky survey plates with a plate measuring machine. The registration should be accurate to an arcsecond. A detailed account of the photometric calibration of the K'-band, J-band and complementary H-band data will be given in Megeath & Herter (1997).

2.2 Millimeter Data

We mapped a subsection of the large K'-band mosaic in 1993 September with the IRAM 30-meter telescope using a 10″ grid spacing. We simultaneously mapped in the $C^{18}O$ $(2\rightarrow1)$, $C^{34}S$ $(3\rightarrow2)$, and $C^{18}O$ $(1\rightarrow0)$ lines. The half power beamwidths were 11″ ($C^{18}O$ $(2\rightarrow1)$), 16″ ($C^{34}S$ $(3\rightarrow2)$) and 22″ ($C^{18}O$ $(1\rightarrow0)$), respectively. In all cases, SIS receivers were used and the resulting system temperatures were 290–563 K, 200–275 K, and 263–353 K in the 1.3, 2, and 3 mm bands, respectively. We observed in a total power mode, taking 2.5 minute integrations and measuring an off position after every 2 on-source positions. The data were calibrated using the chopper wheel method. The spectrometer was an autocorrelator configured to produce 897, 1344, and 896 channel spectra for the 1.3, 2, and 3 mm bands covering 70, 53, and 35 MHz, respectively. The resulting channels were 0.11, 0.08, and 0.11 km s^{-1} wide. Each night we repeated a observations of the center position; the integrated intensity varied by less than 20%.

Pointing corrections were obtained from continuum scans of W3(OH) using the 3 mm receiver. Based on the pointing corrections, the rms pointing error was 3″. However, a measurement of the relative pointing of the 1.3 and 2 mm receivers showed pointing offsets of 4.″7 and 2.″0, respectively. Since we did not monitor this offset over the course of the run, we have not corrected the pointing of the data using the measured offsets. These offsets do not affect any of the conclusions drawn in this paper.

The data were reduced with the CLASS software package. We followed a standard reduction procedure of coadding spectra taken at identical positions and subtracting a first order baseline. We divided the corrected antenna temperatures, T_A^*, by tabulated values of η_{MB} (the beam efficiency divided by the forward efficiency) to place the spectra

[1]The 5 m Palomar Observatory is operated jointly under a collaborative agreement between Cornell University and the California Institute of Technology.

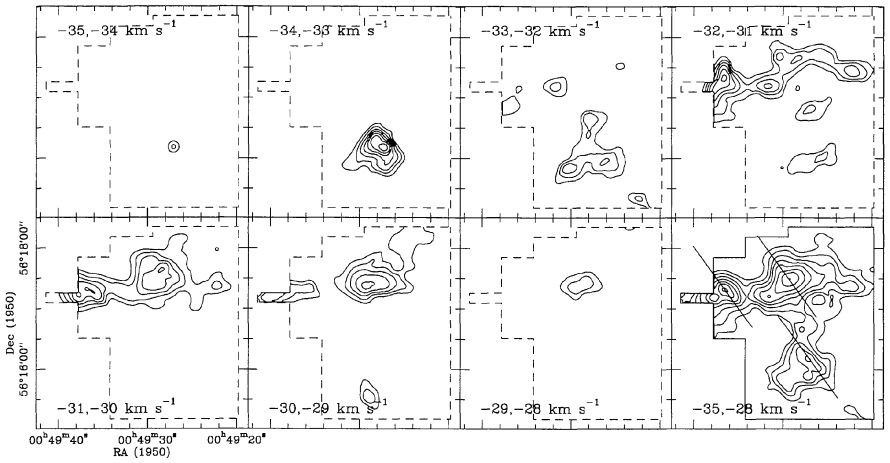

FIG. 3. Channel maps of the $C^{18}O$ (2→1) emission. The levels in the channel maps are 1.98 to 6.60 by 0.66 K km s^{-1}. The lower right panel shows the total integrated emission with contour levels of 5.24 to 17.47 by 1.75 K km s^{-1}. The lines drawn over the integrated emission map show the position-velocity cuts discussed in the text. The channel map shows that the S clump is kinematically distinct from the NW and NE clumps. We find a layer of blueshifted gas along the northern edge of the NW clump. We argue that this layer may have been accelerated by a passing shock front. Similarly, the observed velocity structure in the S clump could also result from a shock.

on a T_{MB} scale. We adopted the standard values of 0.48, 0.58, 0.74 for η_{MB} in the 1.3, 2, and 3 mm bands, respectively. Maps of the spectral line data were produced with the Graphics software package.

2.3 VLA Data

We observed NGC 281 west using the *C*-array configuration of the VLA[2] in 1993 June. To maximize our ability to detect and resolve structures with sizes ranging from an arcsecond to several arcminutes without taking data in several VLA configurations, we observed in the 2, 6, and 20 cm bands using a 50 MHz bandwidth. The phase center was $00^h\ 49^m\ 27.6^s$ and 56° 17′ 41″ (1950). We observed in each band successively, observing the calibrator and then the source in each band. To maximize UV coverage, we returned to NGC 281 after observing a second source and repeated this procedure.

The data were calibrated, transformed, and cleaned in the AIPS package. Initially, we used a uniform weighting. After cleaning, the data were convolved to resolutions of 13″×12″, 4.″3×3.″0, and 1.″2×1.″1. Emission is clearly detected in the 20 cm data. After applying 30 and 20 kλ tapers to the 6 cm data, resulting in 5.″1×3.″8 and 7.″6×6.″6 beamsizes, signal was apparent in the 6 cm data coincident with the peak of the 20 cm emission. Since the emission is extended, the absence of emission at 2 cm and the weak emission at 6 cm is due to the lack of short baselines in these bands. The 20 cm maps are not sensitive to emission extended over 7′, hence much of the emission in the 20′ diameter H II region is absent (see continuum map in Israel 1977). The extended emission results in a ripple which is seen throughout the map. The features reported in this paper are significantly brighter than the ripple.

[2]The National Radio Astronomy Observatory is a facility of the National Science Foundation operated under cooperative agreement by Associated Universities, Inc.

3. RESULTS AND ANALYSIS

3.1 The Structure and Properties of the Molecular Gas

In Fig. 2 (Plate 59), we present the $C^{18}O$ (1→0), $C^{18}O$ (2→1), and $C^{34}S$ (3→2) maps of the ^{13}CO (1→0) peak shown in Fig. 1. While the 47″ resolution FCRAO ^{13}CO (1→0) observations show a single peak, our higher resolution $C^{18}O$ (2→1) and $C^{18}O$ (1→0) maps reveal a complex morphology with considerable fine scale structure. The $C^{18}O$ maps show that the emission is concentrated in three spatially distinct clumps. Hereafter, we will refer to the northeastern clump as NE, the northwestern clump as NW, and the southern clump as S. The $C^{18}O$ integrated intensity maps suggest that the three clumps form a connected structure, with the clumps interconnected by bridges of line emission. However, $C^{18}O$ (2→1) channel maps (Fig. 3) show that clump S is found in the −34 to −32 km s^{-1} channels while clumps NW and NE are found in the −32 to −29 km s^{-1} channels. Accordingly, while clumps NW and NE appear to be a connected structure, clump S is a kinematically and spatially distinct from the northern clumps. The bridge between the NW and S clumps appears to result from the chance coincidence of a fourth, smaller clump found in the −33 to −31 km s^{-1} channels. A number of less intense peaks, as well as emission near the northwestern edge of the maps (see −30 to −29 kms channels in Fig. 3) indicate the existence of additional clumps and components in the maps. In the following discussion, we will concentrate on the NW, NE, and S clumps since they dominate the molecular mass in the region.

We now estimate the masses and H_2 densities of the NW, NE, and S clumps. We start with the ratio of the $C^{18}O$ (2→1) and $C^{18}O$ (1→0) lines, which is a good estimator of volume density if the kinetic temperature, T_K, is known. This is due to the low optical depth in these lines and the independence of the line ratios on distance and abundance. As we show in Fig. 4, the observed $C^{18}O$ (2→1) to $C^{18}O$ (1→0) ratio of all three clumps varies between 2.5 and 3.5.

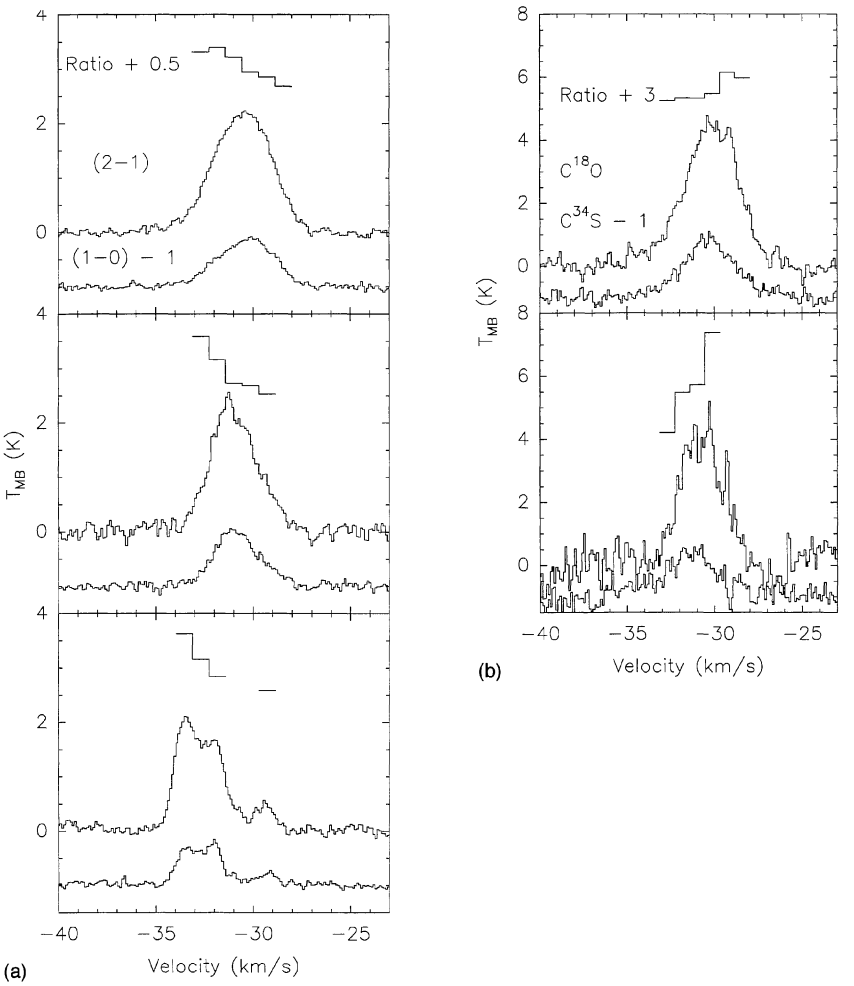

FIG. 4. (a) The $C^{18}O$ (1→0) line, $C^{18}O$ (2→1) line and $C^{18}O$ (2→1) to (1→0) line ratio for the NW (top), NE (middle) and S (bottom) clumps. The lines have been averaged over a 40″×40″ region centered on each of the clumps. To separate the lines, we have added 0.5 to the line ratio and subtracted 1 from T_{MB} of the (1→0) line. In all three cases, the blueshifted gas (relative to the line center) shows a higher line ratio. This is indicative of a higher density and/or temperature in the blueshifted gas. Also, note that the −29 km s^{-1} component in the S clump appears to arise in a separate clump in the line of sight. (b) The $C^{34}S$ (3→2) line, $C^{18}O$ (2→1) line and $C^{18}O$ (2→1) to $C^{34}S$ (3→2) line ratio for the NW (top) and NE (bottom) clumps. The lines have been averaged over the regions of detected $C^{34}S$ (3→2) emission. We have added 3 to the line ratio and subtracted 1 from T_{MB} of the $C^{34}S$ (3→2) line. The ratio is lower for the blueshifted gas; suggesting that the $C^{34}S$ (3→2) emission is preferentially coming from the blueshifted gas.

This ratio is indicative of emission from a warm, optically thin, $C^{18}O$ gas. Given T_K=29 K (Henning *et al.* 1994) and our observed $C^{18}O$ (2→1) to $C^{18}O$ (1→0) ratios of 2.5–3.5 (Fig. 4), the LVG results of Goldsmith *et al.* (1983) predict densities $>2\times10^4$ cm^{-3}. For a density of 2×10^4 and T_K=29 K, the LVG models of Mauersberger *et al.* (1992) predict column densities of

$$N(H_2)\sim 3\times10^{21}\int T_{MB}(C^{18}O,\ J=2\rightarrow1)dv, \qquad (1)$$

where $N(H_2)$ is the molecular hydrogen column density in cm^{-2}, T_{MB} is the main beam brightness temperature in K, and v is velocity in km s^{-1}. This result is not strongly dependent on density or temperature. Using the above relationship, we can calculate total clump masses by integrating the $C^{18}O$ intensity over the spatial extent of each clumps. The resulting masses are 570, >210 and 300 $M_\odot$ for the NE, NW, and S clumps. Note that we determined only a lower limit for the second clump since it was not completely included in our maps. Assuming that the clumps are spherical, we calculate average volume densities of 1.4, >1.0, and 2.0×10^4 cm^{-3}. These densities are slightly lower than the lower limit ($>2\times10^4$ cm^{-3}) determined from the LVG models of Goldsmith *et al.* (1983). The disagreement between the estimates may result from density structure in the clumps or from a higher kinetic temperature ($T_K\sim$40 K).

Emission from molecular transitions with higher critical densities, such as the $C^{34}S$ (3→2) transition, is often taken as evidence for high density gas. In Fig. 7, $C^{34}S$ (3→2) is detected towards parts of the NW and NE clumps. Since $C^{34}S$ (3→2) has a critical density of $\sim5\times10^5$ cm^{-3}, the detection of localized $C^{34}S$ (3→2) in the NW and NE clumps indicates that the NW and NE clumps have peak volume densities which are significantly higher than the derived average volume densities.

In Fig. 4, we plot the spectral lines averaged over each

clump. The lines are broad, indicating that the internal velocity fields are dominated by turbulent and bulk gas motions and not the thermal motion of the gas. The virial relation, $M = k\sigma^2$ where M is the clump mass, k is a constant, and σ is the velocity dispersion, is commonly used to calculate the masses of clumps. The application of this relation assumes that the clumps are virialized and strongly self-gravitating. Bertoldi & McKee (1992) argue that the latter assumption is often not valid for molecular cloud clumps; however, the calculation of the virial mass and its comparison to other mass determination can lead to insights in the properties of the clumps. Specifically, assuming that the masses derived from the $C^{18}O$ measurements are accurate,

$$\frac{M_{virial}}{M_{C^{18}O}} \approx \frac{2T}{|W|} \tag{2}$$

where T is the clump internal kinetic energy and W its gravitational energy. A strongly self-gravitating clump will have a value of $M_{virial}/M_{C^{18}O} \approx 1$. Since the contour maps show that the clumps are moderately centrally condensed, we use the virial relationship for a $1/r$ denisty law as given by MacLaren, Richardson & Wolfendale (1988). We determine that $M_{virial}/M_{C^{18}O}$ equals 1.9, < 3.5, and 2.2 for the NW, NE, and S clumps, respectively. Since the NE clump was not completely included in our IRAM 30 meter map, we have assumed a symmetric intensity distribution in RA. Thus, we find M_{virial} is approximately twice $M_{C^{18}O}$, indicating that the kinetic and gravitational energies are similar. Accordingly, we find that the clumps are either not strongly self-gravitating and may be partially confined by the pressure of an external gas or that they are dynamically perturbed, e.g., by shocks, which enhance the kinetic energy over that expected in virial equilibrium. The latter is likely since the clumps appear to be photoevaporating, and as a result, they may be pertrubed by shocks driven by the high pressure of the ionization fronts (Secs. *3.2* and *3.4*). Alternatively, the clumps may be confined in part by the pressure of the ionization fronts.

3.2 The Relationship of the Molecular Gas to the H II Region: The Evidence for Photoevaporation

In Fig. 5 (Plate 60), we have overlayed the $C^{18}O$ $(2\rightarrow1)$ map over a subsection of the Hα image shown in Fig. 1. The $C^{18}O$ $(2\rightarrow1)$ clumps are in the obscured southwestern quadrant of the nebula. To the northeast of the clumps is the primary source of ionizing UV photons, HD 5005, at a projected distance of 3.8 pc from the NW clump. Directly north of the clumps, a bright limb of Hα is apparent, suggesting that the obscuring molecular cloud is exposed to the UV radiation from the OB stars and is being photoionized. However, the Hα image does not show the ionization front extending to the clumps. This suggests that either the clumps are shielded by a lower density molecular gas or the Hα emission associated with the clumps is obscured by a foreground screen of molecular gas.

The VLA 20 cm image provides a map of the ionization front which is not biased by extinction. The reader should note that the VLA data emphasizes compact structures and edges and that the extended, slowly varying emission has been filtered out. The 20 cm data shows several, distinct regions of compact emission (Fig. 5); we infer from the widespread distribution of the emission that the H II region/molecular cloud interface is not a single edge-on plane. The brightest emission is north of and adjacent to the NW and NE clumps, indicating that the H II region does extend to the two northern clumps. The ridge of bright 20 cm emission associated with the NW and NE clumps is highly suggestive of a flow of photoionized gas streaming off the clumps. Hence, we propose that the NW and NE clumps are protruding into the H II region and are directly exposed to the ionizing UV radiation. Accordingly, the 20 cm emission is tracing the photoionized gas as it expands outward into the surrounding low density H II region.

We also find 20 cm emission directly northward of clump S, suggesting that this clump is exposed or partially exposed to the ionizing UV radiation and is also photoevaporating. This would require either the deep penetration of UV radiation into the cloud or a H II/molecular interface which is inclined so that all three clumps can intrude into the H II region. In comparison to the emission from the NW and NE clumps, the emission north of the S clump is both weaker and smaller in size. We will discuss a possible reason for the small extent and luminosity of this emission in Sec *3.3*. Interestingly, a weak peak of emission is observed at the southern edge of the S clump. This peak may not be associated with the S clump, but could instead result from the photoevaporation of a small, kinematically distinct clump apparent in the -30 to -29 km s^{-1} velocity interval in Fig 3.

To the west of the three clumps, we find a bright region of 20 cm emission. This emission may result from a fourth, photoevaporating molecular clump; however, our 30-meter map did not include this region and we do not have a conclusive detection of the clump. We do find that in the lower angular resolution ^{13}CO $(1\rightarrow0)$ data in Fig. 1, there is an extension of the peak ^{13}CO $(1\rightarrow0)$ emission towards the west, consistent with the presence of a fourth clump to the west of our 30-meter field. In addition, several smaller peaks of 20 cm emission are scattered throughout the H II/molecular interface; these may result from the photoionization of smaller molecular clumps.

3.3 Further Evidence for Photoevaporating Clumps: A Comparison with Theory

In their analytical study of the photoevaporation of a spherical clump, Oort & Spitzer (1955) found that an equilibrium is quickly established in the flow of ionized gas off the clump. In the expanding photoevaporated gas, hydrogen atoms recombine and then absorb incident Lyman continuum photons, and as a consequence, will partially shield the molecular gas from the incident UV radiation. In contrast to a Strömgren-like equilibrium in which all Lyman-continuum photons are absorbed in the H II region, a fraction of the photons can penetrate the photoevaporative flow and reach the molecular gas. These photons ionize the neutral gas at the clump surface and replenish the flow. The ratio of the inci-

dent Lyman continuum flux over the Lyman continuum flux penetrating to a spherical clump's surface is given by q, where

$$q \simeq \left(0.1 \frac{S_{\rm lyc} r \alpha}{4 \pi R^2 c_{\rm II}^2} \right)^{1/2}, \quad (3)$$

where $S_{\rm lyc}$ is the Lyman continuum photon production rate of the OB stars, R is the distance from the OB stars to the clump, r is the radius of the clump, α is the recombination coefficient of the ionized gas, and $c_{\rm II}$ is the sound speed of the ionized gas (B89). Using the spectral types of the HD 5005 trapezium system given in Guetter & Turner (1997) and the relation between spectral type and Lyman continuum photon production rate given in Panagia (1973), we find a total Lyman continuum photon production rate of 1.6×10^{49} s^{-1} for the HD 5005 system. For a distance of 2.94 kpc, the clump radii are 0.5 pc for the NW and NE clumps and 0.4 pc for the S clump and the projected separations from HD 5005 to the NW–NE and S clump surfaces are 3.8 and 5.1 pc, respectively. The resulting values of q are 17 and 11 for the NW–NE and S clumps, respectively. The values of q indicate that most of the incident Lyman-continuum photons are absorbed in the photoionized gas before they reach the neutral clumps. Consequently, if the 20 cm emission is indeed arising in a photoevaporative flow, the measured recombination rate in the flow should be to good approximation equal to the rate of Lyman continuum photons impinging on the clumps.

Assuming that the distances between HD 5005 and the clumps are near the projected separation and using a geometrical cross section equal to the observed total surface area of the NW and NE clump (2×1 pc^2), we calculate that the rate of Lyman continuum photons emitted towards the NW and NE clumps is 1.7×10^{47} s^{-1}. Since the projected distance is a lower limit to the actual distance, the calculated incident Lyman continuum flux is an upper limit. However, since the 20 cm emission is detected primarily *adjacent* to the clumps, the H II/molecular interface must be nearly edge on, and consequently, the actual distance cannot be much larger than the projected distance. Using the case B recombination coefficient, we find that the recombination rate is 1.2×10^{47} s^{-1}. Based on the radio maps of Israel (1977), we estimate that the recombination rate in the intervening H II region is 0.2×10^{47} s^{-1}, and that the total recombination rate (photoevaporative flow plus intervening H II region) is 1.4×10^{47} s^{-1}. Thus, considering the uncertainties in the separation between HD 5005 and the clumps, the total geometric cross section of the NW and NE clumps and the Lyman-continuum production rate of the HD 5005 system, we find the total recombination rate is in surprisingly good agreement with the predicted Lyman-continuum flux.

We now compare the observed and predicted sizes for the 20 cm emission associated with the NW and NE clumps. Since the velocity of photoevaporated gas is approximately constant through most of a photoevaporative flow, the density of the ionized gas flowing away from a *spherical* clump will roughly follow an inverse square law, i.e., $n_e \propto r^{-2}$ where r is the distance to the center of the clump, and n_e is the electron density of the ionized gas (Oort & Spitzer 1955). Since the thickness of the photoevaporative flow scales with r and the electron density drops as $1/r^2$, the resulting surface brightness is $I_\nu \propto n_e^2 l \propto r^{-3}$. Taking into account the beamwidth of the 20 cm data, a simple numerical simulation shows that the surface brightness should decrease by half at 0.2 pc from the peak. We find in the north–south direction, the distance from the peak emission to the half-power contour is 0.3 pc. Thus, we find that the observed emission extends further than the emission calculated for a photoevaporative flow from a spherical clump, but the sizes are within a factor of two. The difference between the observed and predicted values may be due to the combined flow from the NW and NE clumps, which would decrease more slowly than the flow from a single spherical clump.

The 20 cm emission associated with clump S is neither as extended nor as bright as the emission towards the northern clumps. Since the extent of the emission is dependent on the size of the clump, this would imply that the S clump is smaller than the NW or NE clumps (Oort & Spitzer 1955). Although the radius of the S clump is comparable to NW and NE clumps, we find that the surface of the S clump facing the OB stars has a distinctly smaller cross section and radius of curvature (Fig. 5). We estimate that the radius of curvature is $r = 0.2$ pc. This size is roughly comparable to the extent of the associated 20 cm emission. Given the clump geometrical cross section is πr^2, we find that the incident Lyman continuum photon rate is 7.1×10^{45} s^{-1}. From the 20 cm emission north of S, we calculate a recombination rate of 6.2×10^{45}. Including the estimated recombination rate in the intervening H II region based on the map of Israel (1977), we determine a total recombination rate of 8.4×10^{45} s^{-1}. Again, there is a good agreement between the incident UV Lyc rate and recombination rate in the S clump if we adopt a radius of curvature of 0.2 pc. Although a small radius of curvature may explain the weakness of the 20 cm emission at the northern tip of clump S, we note that there is a sizeable protrusion on the eastern face of the clump. This protrusion should also be exposed to the UV radiation from the OB stars, yet we do not detect 20 cm emission near the protrusion. It is possible that the protrusion is shielded from the UV radiation field either by the NW and NE clumps, by a lower density gas not detected in the $C^{18}O$ measurements, or by the S clump itself.

3.4 The Effect of Photoevaporation on the Molecular Gas: Is There a Pressure Equilibrium?

The photoionization of the molecular gas and the subsequent heating of the gas to 10^4 K will result in an increase of pressure at the surface of a photoevaporating clump. The density and pressure of the ionized gas is determined by the flux of ionizing UV photons incident on the molecular gas and the size of the molecular clump. If the pressure exerted by the photoionized gas is higher than the internal pressure of the molecular gas, the photoevaporation leads to the compression of the clump. B89 and LL94 show how the compression of globules by ionization front driven shocks eventually results in pressure equilibrium between the ionized gas and the molecular gas. Thus, a pressure equilibrium between the ionized and molecular gas is indicative of a clump which

was initially too dense to be compressed *or* a clump which has already been compressed by shocks and is now in pressure equilibrium with the ionized gas. Converseley, if the clump pressure is lower than the pressure exerted by the photoionized gas, then it is likely that shocks are progressing through the clump.

The pressure upon the neutral gas arises from the combination of the thermal and ram pressure of the photoevaporative flow, which can be evaluated from the recombination rate and the clump diameter. Using relations in B89 and Bertoldi & Draine (1996), we estimate that the pressure of the ionized gas is 2.5×10^7 cm^{-3} K. Highly non-thermal linewidths are apparent in the NGC 281 clumps, and we expect that the internal pressure of the clumps is dominated by turbulence and not thermal motions. Using the measured linewidths of the clumps, we find that the turbulent pressure of the molecular gas is 1×10^7 cm^{-3} K. The apparent imbalance of pressures should result in the shock compression of the molecular gas. We can determine the shock speed in a clump by the pressure balance between the ram and turbulent pressure of the pre-shock gas and the ram and thermal pressure of the ionized gas,

$$n_0[\mathrm{cm}^{-3}](v^2_{\mathrm{shock}}[\mathrm{km\ s}^{-1}]+\sigma^2_{\mathrm{turb}}[\mathrm{km\ s}^{-1}]) = 7.5\times10^4\left(\frac{R_e}{10^{47}\mathrm{s}^{-1}}\right)^{\frac{1}{2}}\left(\frac{D}{1\,\mathrm{pc}}\right)^{-3/2}, \quad (4)$$

where R_e is the measured recombination rate in the photoevaporating gas, D is the diameter of the clump, n_0 is the density of H_2, σ is the 1D velocity dispersion of the clump, and v_{shock} is the shock velocity. Using the widths of the clump averaged line shapes in Fig. 4, we calculate that $\sigma_{\mathrm{turb}}\sim1.3$ km s^{-1} in all three clumps; the resulting shock speed is 1.4 km s^{-1}. If the clumps were initially strongly self-gravitating and in virial equilibrium, then σ_{turb} of the pre-shock gas would equal ~1 km s^{-1}. The resulting value of v_{shock} is 1.7 km s^{-1}. Thus, over the range of likely values of σ_{turb} and for our best estimates of R_e, n_0, and D, we determine shocks speeds of approximately 1.5 km s^{-1} for all three clumps. The corresponding shock crossing time for the clumps is $\sim$0.7 Myr.

We caution that uncertainties of a factor of two in the molecular and ionized gas densities are possible. Furthermore, magnetic field pressure may also be important in the clumps. Within these uncertainties, it is possible that the molecular and ionized gases may be in a rough pressure balance. Thus we conclude that the observed clump densities and 20 cm fluxes are consistent with either low velocity ($\sim$1.5 km s^{-1}) shocks or pressure balance, with the existence of low velocity shocks being favored by our best estimate of the relevant parameters.

3.5 Clump Kinematics: A Comparison with Radiation Driven Implosion Models

Given the possibility of low velocity shocks, we now examine whether the kinematic structures observed in the clumps could result from shock compression. The clearest signature of a shock is two kinematically distinct components in the molecular line emission. Since the NGC 281 West molecular cloud obscures the optical nebula, the molecular gas is foreground to the NGC 281 nebula. Accordingly, an approximately planar shock would accelerate the gas towards us, resulting in a *blueshifted* post-shock gas component. For spherical clumps, the kinematics can be more complex. Since the pressure of the ionized gas is exerted along a normal to the clump surface, a *converging* shock wave will be driven into the clump. The rapid compression of a clump by a converging shock wave is referred to as a radiation driven implosion (RDI). RDIs were first numerically studied by Sandford *et al.* (1982), and more recently B89 & LL94 published detailed analytical and numerical studies of RDIs in an attempt to understand the origin of cometary shaped globules in H II regions.

There is ample evidence for complex, supersonic velocity structure in the observed clumps. The clump averaged line shapes are clearly non-Gaussian (Fig. 4). There is also evidence for multiple components in the channel maps of the $C^{18}O$ (2$\rightarrow$1) emission (Fig. 3). In the channel maps, we find a layer of blueshifted emission (-32 km s^{-1} to -31 km s^{-1}) at the northern edges of the NW and NE clumps adjacent to the 20 cm emission. The NW clump exhibits a clear velocity gradient with an increasingly blueshifted velocity with increasing declination; the blueshifted gas could be tracing a layer of post-shock gas. The channel maps show a similar velocity gradient in the S clump with most of the clump moving at the blueshifted velocity.

For a comparison with RDI models, in Fig. 6 (Plate 61) we present position-velocity (PV) diagrams for slices through the NE, NW, and S clumps (the slices are defined in Fig. 3). We have oriented the slices so that they are approximately aligned with the axis of potential RDIs, the axis being defined by the vector from the UV source to the clump center. In each clump, we find complex velocity structure which may be the result of shocks interacting with the clumps. The interpretation of the PV diagrams is difficult without detailed modeling, so we limit our analysis to qualitative comparisons with published numerical results. LL94 presented numerical simulations of PV diagrams for a clump at four evolutionary stages of a RDI, which we now describe assuming a geometry in which the clump is slightly foreground to the OB stars. In stage 1, or the collapse stage, the converging shock is in the process of crossing the clump. Two kinematic components are apparent in this stage's PV diagram: the pre-shock gas at the systemic velocity of the clump and a distinct blueshifted shock component. Very broad lines are evident at the head of globule, due to the shock wrapping around the globule surface. Stage 2 occurs when the shock has crossed the clump and the resulting compression has reached a maximum along the central axis of the implosion. At this time, the post-shock gas furthest from the axis of the implosion has overtaken the slower moving post-shock gas on the implosion axis and is converging behind the globule. This gives the globule a swept back appearance. The velocity difference between the periphery and center of the clump results in a velocity gradient with an increasingly blueshifted velocity with increasing distance from the UV source. A small red-

shifted wing may also be apparent. During stage 3, the overcompressed clump rebounds, resulting in the expansion of the compressed molecular gas. In this stage, the same velocity gradient observed in stage 2 is apparent, with the addition of a strong redshifted wing resulting from the expansion. Stage 4 is the final outcome of the RDI in which the compressed globule reaches a pressure equilibrium with the ionized gas resulting in a cometary globule. In this final stage, the multiple components, velocity gradient, and/or wings are no longer present.

Given the evidence for complex structure and broad linewidths in the PV diagrams, these do not provide a good match to the equilibrium cometary globule stage (stage 4). We now examine each clump for the kinematical features characteristic of the first three stages:

Clump S: A distinct double component (33.5 km s^{-1} and 32 km s^{-1}) is apparent. The blueshifted component (i.e., the proposed post-shock gas) extends to a higher declination than the systemic component, which is consistent with a shock advancing from north to south. Thus, we find that clump S shows the velocity structure characteristic of the collapse stage (stage 1).

Clump NW: The lines in clump NW are broad and there is a hint of two components at 30.5 km s^{-1} and 29.5 km s^{-1} (declination $-10''$). Like the S clump, the blueshifted component extends to a higher declination. Hence, we find that the NW clump is most consistent with the collapse stage (stage 1) of the RDI models, but we note that the two kinematical components are not clearly separated in the PV diagrams.

Clump NE: The $C^{18}O$ (1→0) line in this clumps does show a velocity gradient and a weak redshifted wing, both of which are suggestive of stage 2. Thus, on the basis of the $C^{18}O$ (1→0) PV diagram, we find that the NE clump most closely resembles stage 2. However, the same gradient is *not* apparent in the $C^{18}O$ (2→1) line, which shows a broad line with two separate components (31.5 km s^{-1} and 30.5 km s^{-1}) indicative of stage 1. We suggest that the NE clump is still in the collapse stage (stage 1), but that it is approaching maximum compression (stage 2).

In summary, we find that numerical models of imploding spherical clumps can approximately reproduce the kinematic features observed in the NGC 281 West clumps. However, it is not clear whether the observed motions can be *uniquely* interperted as RDIs. Molecular clouds typical exhibit complex velocity fields. In many molecular clouds, H II regions and outflows from embedded stars may cause the observed velocity structure; however, there may also be other sources of turbulent energy such as clump–clump collisions and the transport of energy from large scale molecular cloud motions to smaller scale motions in clumps. Consequently, we cannot uniquely ascribe the observed kinematics of the clumps to RDIs. However, RDIs remain a plausible and attractive physical model linking the observed photoevaporation to the internal clump kinematics.

3.6 On the Origin of the Dense Gas

We now consider the possibility that shock compression may result in the localized regions of dense gas traced in the $C^{34}S$ (3→2) map. In support of a shock compression origin, the $C^{34}S$ (3→2) emission in the NW and NE clumps shows a similar velocity to the blueshifted $C^{18}O$ emission (Figs. 4 & 6), suggesting that the $C^{34}S$ (3→2) emission may arise in the post-shock gas. Furthermore, the $C^{34}S$ (3→2) emission is confined to two small regions near the symmetry axis of the $C^{18}O$ clumps (Fig. 2). Models predict that the maximum compression of an RDI occurs along the symmetry axis (B89; LL94). As an RDI progresses into the clump, the region of maximum compression created by shock convergence follows the shock front and moves from the front to the rear of the clump (LL94). In the NW clump, we find that the position of the $C^{34}S$ (3→2) emission (declination offset $-5''$) is slightly north of the broadest $C^{18}O$ (2→1) and $C^{18}O$ (1→0) linewidths (declination offset $-10''$: Fig. 6). Hence, the observed morphology and velocity emission is consistent with a converging shock which is currently passing through the center of the clump. This result is in agreement with our conclusion drawn from the $C^{18}O$ PV diagrams (Stage 1 in Sec. *3.5*). In contrast, the $C^{34}S$ (3→2) emission in the NE clump (declination offset $-25''$) is detected south of the peak $C^{18}O$ (2→1) emission (declination offset $-15''$) and $C^{18}O$ (1→0) emission (declination offset $-20''$). This is consistent with a shock which has passed through most of the clump (stage 2 in Sec. *3.5*). Again, this is in agreement with our analysis of the $C^{18}O$ PV diagram for the NE clump.

Although the morphology and kinematics of the $C^{34}S$ (3→2) emission is suggestive of a gas compressed by an RDI, the question remains whether the ~1.5 km s^{-1} shock speeds inferred for the clumps are sufficient to compress the gas to the densities needed to excite the $C^{34}S$ (3→2) transition. For a planar isothermal shock, the compression is given by $\rho_{\rm post-shock}/\rho_{\rm pre-shock}=(v_{\rm shock}/\sigma)^2$. As suggested by Elmegreen *et al.* (1995), we have used the turbulent velocity dispersion, σ, instead of the thermal velocity dispersion. If we assume that the clumps were initially virialized with $\sigma_{\rm turb}\sim 1$ km s^{-1}, resulting in a shock speed of 1.5 km s^{-1} (see Sec. *3.4*), then we would expect a factor of three compression or a post-shock density of $\sim 5\times10^4$ cm^{-3}, which is significantly less than the critical density of the $C^{34}S$ (3→2) transition (5×10^5 cm^{-3}).

The converging shock of an RDI can produce a much higher compression than a plane-parallel shock (Sandford *et al.* 1982; B89). While the compression for a plane parallel shock varies as M^2, where M is the mach number of the shock, the compression of a converging shock can be as high as $\rho_{\rm post-shock}/\rho_{\rm pre-shock}=M^4$. Thus, for a shock speed of 1.5 km s^{-1} and a pre-shock linewidth of 1 km s^{-1}, the turbulent Mach number is $M=1.5$ and the resulting gas density is 1×10^5, which is 1/5 the critical density of $C^{34}S$ (3→2). Furthermore, in localized regions of a turbulent media, the turbulent motions are reduced. In numerical simulations of shocks progressing into a turbulent media, Elmegreen *et al.* (1995) find that in localized regions the compression is given by the *thermal* mach number squared. Considering that the thermal velocity dispersion is ~0.5 km s^{-1}, *converging* shocks progressing into such localized regions ($M^4=81$) could produce densities in excess of 5×10^5 cm^{-3}.

In summary, we find the morphology and kinematics of

the observed $C^{34}S$ (3→2) emission in the NW and NE clumps are suggestive of the dense globules produced along the symmetry axis of an RDI (B89). We also find that compression by a converging, low velocity shock may produce the densities needed to excite $C^{34}S$ (3→2) emission. It is intriguing to speculate that the common appearance of CS emission on the edges of molecular clouds may be the result of the *compression* of pre-existing clumps by external UV fields. This would provide an alternative to the proposal that the dense gas results from the *gravitational* collapse of layers of molecular gas swept up by expanding H II regions.

3.7 A Thermal Gradient in the Molecular Gas?

A remarkable feature of the PV diagrams is the declination offset between $C^{18}O$ (2→1) and $C^{18}O$ (1→0) emission in all three clumps. In the clumps, the blueshifted $C^{18}O$ (2→1) emission is enhanced near the H II region relative to the blueshifted $C^{18}O$ (1→0) emission (Fig. 6). In addition to the positional offset between the $C^{18}O$ (2→1) and $C^{18}O$ (1→0) emission, the spectral lines averaged over each clumps (Fig. 4) show that the blueshifted emission in each clump has an enhanced $C^{18}O$ (2→1) to $C^{18}O$ (1→0) ratio. The higher $C^{18}O$ (2→1) to $C^{18}O$ (1→0) ratios are indicative of a higher density and/or temperature in the blueshifted gas. Given the evidence that the blueshifted emission arises in compressed post-shock gas, shock compression could explain the enhanced $C^{18}O$ (2→1) to $C^{18}O$ (1→0) ratios. However, shock compression cannot explain the declination offset between the $C^{18}O$ (2→1) and $C^{18}O$ (1→0) emission *within* the blueshifted (i.e. proposed post-shock) gas. Instead, we find it more likely that the offset is due to the radiative heating of the clumps by the nearby OB stars. For the gas within a few A_V of the clump surface, photoelectric heating from dust grains will be the dominant source of heating, while the radiative heating of dust grains and the subsequent transfer of the energy to the gas through gas-grain collisions can heat the gas deeper in the clumps (Tielens & Hollenbach 1985). Since both types of heating would be strongest near the surfaces of the clouds exposed to the radiation field of the OB stars, the $C^{18}O$ (2→1) emission would be enhanced near these surfaces. Why is the offset seen primarily in the blueshifted gas? If we attribute the blueshifted line emission to the post-shock gas, then the post-shock layer will be more affected by photoelectric and radiative heating simply because it is closer to the ionization front. Not only would the offset be more pronounced in the blueshifted gas, but the preferential heating of the post-shock gas would lead to the higher $C^{18}O$ (2→1) to $C^{18}O$ (1→0) ratios found in the averaged spectral lines.

3.8 The Stellar Cluster

The wide field K'-band mosaic (Fig. 7) (Plate 62) clearly shows a cluster of stars towards the center of the field. Megeath (1994) showed that the cluster is populated primarily by low mass ($M<2$ $M_\odot$) stars. The most striking feature of the cluster is its division into distinct northern and southern sub-clusters. Between the two sub-clusters is a gap almost totally devoid of stars. This division is seen in Fig. 8,

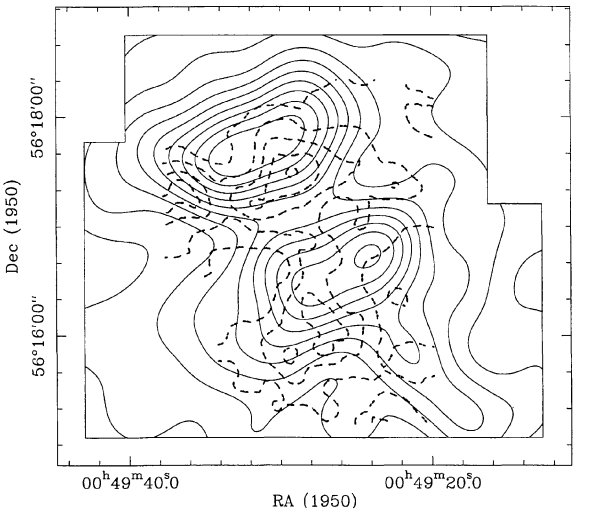

FIG. 8. The solid lines show the stellar density smoothed with a gaussian kernel. The σ of the gaussian is 15″. The contours range from 10 to 100 by 10 stars per pc^{-2}. The dashed line shows the value of A_K determined from the $C^{18}O$ (2→1) column densities with contours of 1.0 to 5.6 by 1.15 mags. The stellar density contours show that the cluster is divided into distinct northern and southern sub-clusters. If the gap between the northern and southern sub-clusters were the result of extinction, we would expect the extinction to peak between the two sub-clusters. Instead, the extinction peaks in the northern sub-cluster, indicating that the gap is due to an absence of stars and that the two sub-clusters are two spatially distinct stellar groups.

in which we present a map of the density of K' sources. Solely on the basis of the K' data, it is not clear whether the cluster consists of two spatially distinct groups of stars or whether the central region of the cluster is obscured by a dense dust lane.

To obscure a section of the cluster would require several magnitudes of extinction in the K'-band, or several tens of magnitudes of extinction in the V-band. In Fig. 8, we have overlayed a map of the K'-band extinction calculated from the derived $C^{18}O$ (2→1) column densities (Sec. *3.1*). We find that the NW and NE clumps obscure part of the gap; however, we do *not* find high extinctions extending throughout the gap. Instead, we find regions in the gap where there are stars and less than one magnitude of extinction in the K'-band. Since we expect that regions with a high enough column density of gas and dust to obscure the cluster will be traced by the $C^{18}O$ (2→1) emission, we must conclude that the gap between the clusters is due to a lack of stars. Given the lack of extinction, one might expect the gap should be contaminated by background field stars; however, there is an exceptionally low incidence of field star contamination in the mosaicked region due to NGC 281's high galactic latitude and location in the outer galaxy.

We conclude that the northern and southern sub-clusters are indeed physically separate sub-clusters resulting from distinct star forming events. Based on the locations of the sub-cluster, the northern sub-cluster appears to be associated with, and partially embedded in the NW and NE clump. Correspondingly, the location of the southern sub-cluster suggests that it is associated with the S clump. This data is indicative of a mode of cluster formation in which star formation is occuring approximately simultaneously in at least

three, separate clumps. As the stars leave the clumps and disperse, they intermingle and form a more extended cluster. Thus, the NGC 281 West cluster may take on a progressively more homogeneous appearance.

3.9 The Impact of Photoevaporation on Star Formation: The Dispersal of the Molecular Gas

We now concentrate our attention on the distribution of stars in the northern sub-cluster. The deep J and K'-band images in Fig. 9 (Plate 63) show that the sub-cluster extends from the H II region into the center of the NW clump. NIR *JHK*-band photometry (Megeath & Herter 1997) shows a clear trend in the colors of the stars, with the reddest source coincident with the $C^{18}O$ $(2\rightarrow1)$ clumps and the bluest stars found in the ionized gas north of the clumps. This trend is also apparent in a comparison of the J and K' images in Fig. 9. The stars coincident with the clumps are typically not detected in the J-band, indicating that they are extremely red. In contrast, the stars northward of the clumps are detected in both the J and K-bands. Since the extinction dominates the colors of embedded young stars, this trend in color shows that the stars towards the clumps are deeply *embedded* in the clumps (or perhaps *behind* the clumps if the stars are very luminous) and that the stars in the H II region show moderate to little extinction (Megeath 1994).

The evidence for an embedded population in conjunction with the existence of an H_2O maser indicates that cluster formation is ongoing in at least the NW clump. However, through photoionization, the clumps are being slowly evaporated and the mass available for star formation is continually declining. Furthermore, photoevaporation driven shocks can sweep up the molecular gas. These shocks can efficiently remove the parental gas surrounding young stars. The extension of the northern sub-cluster into the H II region suggests that part of the cluster has already been cleared of its parental gas by photoevaporation and shocks. If the photoevaporation does not cease, eventually the clumps will be dispersed and star formation will cease. At the current rate of photoevaporation, the complete dispersal of the clumps will require 2.5 Myr. This lifetime may exceed the main sequence lifetimes of the ionizing OB stars; hence, a fraction of the molecular mass of each clump may survive photoionization. The remaining clumps, however, may ultimately be subjected to supernovae. We should note that the formation of massive stars in the clumps may hasten the disruption of the clumps through internal winds and H II regions. Evidence for a deeply embedded 10^4 $L_\odot$ source in the NW clump suggests that the formation of such massive stars may already be occurring (Henning *et al.* 1994). Hence, the ultimate disruption of the clumps and the cessation of star formation may occur prematurely due to the influence of these young massive stars.

3.10 The Impact of Photoevaporation on Star Formation: The Asymmetric Distribution of Stars in the Northern Sub-Cluster

An intriguing feature of the northern sub-cluster is that the center of the sub-cluster is offset from the centers of the NW and NE molecular clumps; the stars are seen primarily in the northern halves of the clumps and in the 20 cm emission to the north of the clumps. This is most apparent in the deep K'-band images, Fig. 9, which show a dense cluster of stars coincident with the northern edge of the NW and NE clumps and with the center of the NW clump. In contrast, the southern edges of the clumps are almost devoid of stars, and only in the southwestern corner of Fig. 9, do we begin to see the stars of the southern sub-cluster. Thus, although the $C^{18}O$ emission shows an approximate north–south symmetry relative to the peak emission, the distribution of observed stars is distinctly asymmetric.

Could the observed asymmetric distribution result from interclump extinction? A map of the interclump extinction calculated from the $C^{18}O$ $(2\rightarrow1)$ data is shown in Fig. 8. Although the extinction through the NW and NE clumps is high enough to obscure stars deeply embedded in the clumps (or on the far sides of the clumps), the observed asymmetry still requires that any population of stars in the southern halves of clumps be more deeply embedded than the observed population in the northern halves of the clumps. Furthermore, stars at the southern edges of the clumps, where the interclump extinction is low, cannot be hidden; consequently, there must be a higher density of stars at the northern edges of the clumps than at the southern edges of the clumps. We conclude that the observed distribution is inconsistent with an isotropic distribution of stars in the molecular clumps. Although extinction certainly affects the observed distribution of K' sources in the clumps, an asymmetric distribution of stars is needed to produce the observed asymmetry.

Since the stars in the NW and NE clumps are concentrated on the edges of the clumps facing the OB group, we find it likely that the asymmetrical distribution of stars is the result of the photoionization of the clumps and/or the resulting dynamical disturbance of the clumps. We summarize here three possible processes:

(i) Clump acceleration: In this scenario, the observed stars formed spontaneously in the observed clumps. After a period of sustained star formation the clumps emerged into the H II region and were exposed to the UV field from the external OB stars. The resulting rocket effect accelerated the molecular clumps away from the OB stars. The stars, which are only coupled to molecular gas through gravity, lag behind (Bertoldi *et al.* 1993). For this scenario to work, the shocks driven by photoevaporation must have already passed through the clump.

(ii) Unveiling through photoevaporation and shocks: this scenario presupposes that spontaneous star formation has recently been occurring throughout the clumps and that the stars are still enshrouded in dense envelopes of infalling gas. The extinction from these circumstellar envelopes hides the young stars from near-infrared observations. The stars remain hidden until the ionization-shock fronts driven into the clumps overtake the stars. Some envelopes may be stripped by the passage of the shocks, leading to the appearance of stars *within* the clumps, as is seen towards the NW clump. The envelopes which survive the shocks will be photoevaporated as the stars emerge into the H II region. Consequently,

the unveiled stars will be confined to the post-shock gas and the neighboring H II region.

(iii) Shock triggered star formation: in this scenario, the formation of the observed stars has either been initiated or accelerated by the compression of gas by the shock wave. Hence, the observed stars are confined to the post-shock gas. After formation, the stars are eventually overtaken by the ionization front and emerge into the H II region. At this point, photoevaporation may also play a role in disrupting circumstellar envelopes.

The key to distinguishing between these scenarios is establishing whether shocks do exist in the clumps. We have presented evidence for shocks in the three clumps; however, further observations are needed to confirm the existence of shocks. If we accept the current evidence for shocks, then the triggered star formation scenario is the best explanation of the observed asymmetry for the following reasons. First, the acceleration of the clumps requires that the shocks have already crossed the clumps; hence, the existence of ongoing shocks rules out the clump acceleration scenario. Second, as we will now argue, the unveiling scenario appears to be inconsistent with the calculated shock crossing time.

The premise of the unveiling scenario is that the clumps are filled with young stellar objects still embedded in their prenatal, collapsing envelopes. For isolated stars, it is thought that the accretion phase is typically terminated by the destruction of the envelope by winds from the central star. However, as has been suggested by Hester *et al.* (1996), the envelopes can also be dissipated by their direct exposure to the UV radiation from external OB stars. It may also be possible for ionization front driven shocks to strip away such envelopes. Accordingly, we have two competing effects: the destruction of the envelopes by internal winds, which operates on a timescale of $t_{\rm wind}$ and the destruction of the envelopes by ionization-shock fronts, which operates on a timescale of the shock crossing time, $t_{\rm shock}$. If $t_{\rm wind} \gg t_{\rm shock}$ then the termination of accretion by the ionization-shock front will be more important, and the unveiling scenario is viable. On the other hand, if $t_{\rm wind} \ll t_{\rm shock}$, then the embedded stars would unveil themselves *before* the ionization-shock front crossed the clump, and consequently, unveiling could not account for the observed asymmetry.

The embedded, accretion phase is thought to correspond to the Class I and Class O objects detected in *IRAS* and submillimeter observations of dark clouds. Studies of the Taurus and Ophiucus regions indicate that the total lifetime of the Class O and Class I phases is <0.3 Myr, after which the stars unveil themselves (Kenyon *et al.* 1990; Greene *et al.* 1994). Thus, on the basis of existing surveys of nearby star forming regions, we find that $t_{wind} < 0.3$ Myr. In comparison, the shock crossing time of 0.7 Myr derived in Sec. *3.4* is somewhat larger than t_{wind}. However, the evidence presented for shocks in Sec. *3.5* suggests that the shocks may have crossed only 1/2 of the NW clump. Consequently, the emergence of the clumps into the H II region and the onset of the shocks may have occurred as recently as 0.3 Myr. Nevertheless, stars which formed before onset of shocks should have already been unveiled by internal winds. Thus, if there is a large population of stars still enshrouded in their prenatal envelopes, these stars must have formed after the emergence of the clumps into the H II region. This would require the formation of the sub-cluster on a timescale shorter than t_{shock}. It is unlikely, however, that a clump could spontaneously form a rich cluster of stars on a timescale which is less than the turbulence crossing time. Consequently, we find it much more likely that a synchronizing impulse, such as a shock, is responsible for the rapid formation of the cluster and the observed asymmetry in the NW and NE clumps.

The southern sub-cluster and clump S show a distribution similar to the northern sub-cluster and the NW and NE clumps. The northern and western portions of clump S contain stars while the southeastern portion appears empty. Furthermore, one of the stars coincident with the northern edge of clump S is surrounded by a faint nebulosity, suggesting that it is still associated with the clump. However, the overall relationship between the southern sub-cluster and clump S is less clear. In particular, the southern sub-cluster is much more extended in the east–west direction than clump S, suggesting that other clumps may also have contributed to the sub-cluster. These clumps may have since been fully evaporated. Since we do not have deep *JHK′* images of clump S, a more detailed study of the southern sub-cluster is needed.

3.11 The Impact of Photoevaporation on Star Formation: Evidence, Mechanisms and Time Scales for Triggered Star Formation

The evidence for triggered star formation is based on an inferred causal connection between photoevaporation, crossing shock fronts, and the asymmetry in the distribution of stars, and the strength of the evidence relies on the individual strengths of these three foundations. Although we have not measured the velocity of the ionized gas, we find the evidence for photoevaporation quite compelling. This is particularly true for the NW and NE clumps. The evidence for shocks is weaker since interperting the kinematics of turbulent clumps is difficult. Higher resolution $C^{18}O$ observations using millimeter interferometers may enhance the case, but the interpretation of such data may still be difficult due to the comparable magnitudes of the inferred shock velocities and the observed turbulent linewidths in the clumps. Thus, we suspect that the umambiguous identification of low velocity shocks will remain difficult. Finally, we find that the evidence for an asymmetrical distribution of stars in the NW and NE clumps is substantial. Deeper K' observations and sensitive mid-infrared imaging from space based platforms will place stronger constraints on the distribution of embedded young stellar objects. In total, we find that there is substantial evidence for triggered star formation in the NW and NE clumps. Future observations promise more stringent tests of the triggered star formation scenario.

The original mechanism for triggered star formation in NGC 281 proposed by Elmegreen & Lada (1978) was the "collect and collapse mode." In their scenario, the observed peak in the column density at the edge of molecular cloud was the result of the gravitational collapse of an unstable layer of swept-up molecular gas. In support of this mechanism, Elmegreen & Moran (1979) interpreted a velocity shift in their 2.3′ resolution ^{12}CO $(1 \rightarrow 0)$ and ^{13}CO $(1 \rightarrow 0)$ data

as evidence for a large-scale shock-wave sweeping up the lower density gas. We find no evidence for such a shock in our data. The reported velocity shift may be explained by the lower resolution of their data and the velocity difference we have observed between the NW-NE and S clumps. Thus, although there is evidence for triggered star formation in our data, the mechanism appears to be the compression of pre-existing clumps through smaller-scale shocks and not the large-scale gravitational collapse of swept-up molecular gas.

B89 proposed that star formation triggered by an RDI would occur along the symmetry axis in highly compressed gas created by the converging shock front. We find that such compression may be occurring in the NGC 281 clumps and may give rise to the observed $C^{34}S$ (3→2) emission; however, it is unlikely that star formation in the NW and NE clumps is confined to the observed $C^{34}S$ (3→2) emission regions. Although we detect a group of stars coincident with the $C^{34}S$ (3→2) emission in the NW clump, we find that the observed stars are spread across the northern rims of the NW and NE clumps. Consequently, if star formation is being triggered, the compression of gas along the symmetry axis of the implosion cannot be the only mechanism. Since star formation requires dense gas, we suggest that much of the dense gas may be found in density enhancements much smaller than our beamize. These may be pre-existing enhancements which are compressed by the passing shocks, and the $C^{18}O$ clumps may then contain many small converging shock fronts which are unresolved by millimeter observations. The compression of these peaks could result in the formation of individual stars or small stellar groups. Further theoretical work is needed to examine the propagation of shocks in inhomogeneous, turbulent clumps.

If star formation is being triggered by ongoing shock compression, then the formation must occur on a timescale shorter than roughly half the shock crossing time (~0.3 Myr). If densities in excess of 10^5 cm^{-3} are obtained in localized regions of the compressed post-shock gas, then the resulting free fall time onto a central protostar will be less than 0.1 Myr. Furthermore, to accrete ~1 $M_\odot$ on a timescale <0.3 Myr, accretion rates in the forming NGC 281 West cluster must not substantially exceed 10^{-5} $M_\odot$ yr^{-1}, which is the typical accretion rate inferred for young, solar mass stars in nearby dark clouds. Hence, our observations do not require an unusually short collapse times or high accretion rates. Perhaps, the main role of the shock is to trigger the collapse of existing prestellar mass cores or to concentrate the gas into prestellar dense cores which then collapse. We do find that the collapse time required by the triggered star formation scenario is much smaller than the ambipolar diffusion timescale. This suggests that ambipolar diffusion does not control the formation of prestellar cores in NGC 281 West. Interestingly, the youth inferred for many young clusters suggests that ambipolar diffusion does not play an important role in regulating the formation of dense clusters in general.

Finally, we estimate the star formation efficiency in the northern sub-cluster. We assume that the stars form in the shocks and then enter the H II region as the parental gas is photoevaporated. We can then measure the mass of molecular gas from which the stars formed by estimating the mass of the photoevaporated gas. On a timescale of 0.3 Myr (1/2 the shock crossing time of the NW clump), ~50 $M_\odot$ of the NW and NE clumps would have photoevaporated. In the H II region north of the NW and NE clumps, we find ~100 stars (Fig. 9). Given an average stellar mass of ~0.5 $M_\odot$, the resulting star formation efficiency is ~50%. This implies that if star formation is being triggered by shocks, then the resulting star formation process must be extremely efficient.

4. CONCLUSIONS

We present an analysis of the interface between the NGC 281 H II region and the NGC 281 West molecular cloud from an intercomparisons of newly obtained VLA 20 cm data, $C^{18}O$ (1→0), $C^{18}O$ (2→1) and $C^{34}S$ (3→2) maps, and near-infrared imaging. With this data, we have studied the relationship between the molecular gas, ionized gas, and associated stellar population in the H II/molecular cloud interface in detail. The main findings of our study are:

- We have resolved the molecular gas near the H II region/molecular cloud interface into three clumps, NW (northwest), NE (northeast) and S (south). The NW and NE clumps appear to form a connected structure, but the S clump is spatially and kinematically distinct. The clump masses determined from the $C^{18}O$ (2→1) derived column densities are 570, >210, and 300 $M_\odot$, and the implied average volume densities are 1.4, >1.0, and 2.0×10^4 cm^{-3} for the NW, NE, and S clumps respectively. Emission in the $C^{34}S$ (3→2) line is detected towards the NW and NE clumps, indicating the presence of dense (~5×10^5 cm^{-3}) gas.
- The kinetic and gravitational energy of the clumps appear to be approximately equal, indicating that the clumps are not strongly gravitationally bound. This suggest that the clumps are either confined by an external pressure (perhaps a photoionized gas at the clump surface) or that they have been perturbed by shock compression.
- VLA 20 cm imaging shows emission from ionized gas at the northern edge of each clump. The strongest emission is seen adjacent to the NW and NE clumps. We propose that all three clumps are exposed to the UV radiation from the OB stars ionizing the NGC 281 nebula. The luminosity and extent of the ionized gas is consistent with the predictions of theoretical models of photoevaporative flows.
- We have compared the external pressure of the photoevaporating gas to the internal turbulent pressure of the clumps, and find that the external pressure is a factor 2.5 higher. Within the uncertainties inherent in determining the external and internal pressures, we find that there may be a pressure equlibirium, but our best estimates of the clump and photoevaporation parameters favor the existence of low velocity (1.5 km s^{-1}) shocks.
- Examination of the spectral line profiles and channel maps reveals complex kinematical structures which may arise in shocks. We have compared position-velocity diagrams in the $C^{18}O$ (2→1), $C^{18}O$ (2→1), and $C^{34}S$ (3→2) lines with published models of radiation driven implosions (RDIs). We find that ongoing RDIs can explain much of the velocity structure observed in the clumps. However, we note

that clumps in molecular clouds often show complex turbulent motions, and accordingly, it is difficult to uniquely ascribed the observed motions to RDIs.

• The velocity and the morphology of the observed $C^{34}S$ (3→2) emission are consistent with the emission arising in highly compressed gas created by the converging shock waves passing through the NW and NE clumps. Accordingly, we suggest that the dense gas traced by $C^{34}S$ (3→2) in NGC 281 West may have resulted from compression by RDIs.

• Variations in the $C^{18}O$ (2→1) to $C^{18}O$ (1→0) line ratio with position and velocity in the clumps are most likely the result of temperature gradients in the clumps. The highest $C^{18}O$ (2→1) to $C^{18}O$ (1→0) ratios (corresponding to a higher temperature gas) are found near the H II region, suggesting that the OB stars are radiatively heating the clumps.

• Near-infrared imaging reveals a dense cluster of low-mass stars. From the distribution of the associated stellar population and the molecular gas, the cluster is divided into northern and southern sub-cluster. The two sub-clusters appear to be the result of at least two independent star forming events; one of which appears to be ongoing in the NW and NE clumps, and the other of which may be associated with the S clump.

The photoevaporation will eventually disrupt the clumps and terminate ongoing star formation. The extension of the northern sub-cluster into the H II region suggests that photoevaporation and shocks have already partially cleared the parental gas of the sub-cluster. We calculate that the NW and NE clumps will be fully evaporated on a timescale of 2.5 Myr. However, there is some evidence for the ongoing formation of massive stars in the NW clump. These stars would significantly hasten the disruption of the clumps.

• In the northern sub-cluster, the stars detected in deep K' imaging are found either in the northern halves of the NW and NE clumps or in the adjoining H II regions; the southern halves of the clumps contain only a few sources. We have considered three hypothesis for the observed asymmetry in the distribution of stars: (1) the gas clumps have been accelerated relative to the stars by photoevaporation (the rocket effect), (2) the stars are hidden to near-infrared observations by dense, circumstellar envelopes until the envelopes are disrupted by the passage of the stars through an ionization-shock front, (3) a shock wave is triggering the collapse of the molecular gas and the resulting stars are confined to the post-shock gas.

• If we accept evidence for *ongoing* shocks in the clumps, then we find that the shock triggered star formation scenario is the best explanation of the observed asymmetric distribution of stars in the NW and NE clumps.

Note Added in Proof: We have recently extended our map of NGC 281 West in the $C^{18}O$ (2→1), $C^{34}S$ (3→2), and $C^{18}O$ (1→0) transitions with the IRAM 30-meter telescope (1997 July). The new map shows several clumps coincident with the western 20 cm emission (R.A. $00^h\ 49^m\ 15^s$), supporting our claim that this 20 cm emission is tracing gas photoevaporating off of clumps not covered in our 1993 map (Fig. 2). Furthermore, towards the NE clump, our new map shows that the $C^{18}O$ emission drops precipitously to the east of the clump and does not extend further east than the adjacent ridge of 20 cm emission. Again, this supports our claim that the 20 cm emission north of the NE clump is tracing gas photoevaporated from the clump. Finally, we have confirmed the weak $C^{34}S$ (3→2) emission towards the NE clump; however, the emission is roughly a factor of five weaker than the emission shown in Fig. 2. The $C^{34}S$ (3→2) emission towards the NW clump shows a comparable strength to our 1993 measurements.

We are greatly in debt to John Rayner for generously his sharing observing time and his wisdom, to Kiriaki Xilouris for obtaining the Hα image at the Skinakas observatory (Crete), and to Frank Bertoldi for vastly improving our understanding of photoevaporation and radiation driven implosions and for commenting on several drafts of this paper. An anonymous referee returned a number of detailed commentswhich also improved the quality of this paper. We also thank John Carpenter, who supplyed us with his CO and CS data, and Tom Herbst, who measured the positions of stars on the Palomar plates which we used for our registration. Finally, we acknowledge the excellent support of the staffs of the IRAM 30 m, the VLA, the University of Hawaii 2.2 m, and the Palomar 5 m. During the duration of this work, STM held a fellowship at the Max–Planck–Institut für Radioastronomie and subsequently, an MIT/CFA fellowship at MIT Haystack observatory.

REFERENCES

Bertoldi, F. 1989, ApJ, 346, 735 (B89)
Bertoldi, F., & McKee, C. F. 1990, ApJ, 354, 529
Bertoldi, F., & McKee, C. F. 1992, ApJ, 395, 140
Bertoldi, F., McKee, C. F., & Klein, R. I. 1993, in Massive Stars: Their Lives in the Interstellar Medium, edited by J. Cassinelli and E. Churchwell (ASP, San Francisco), p. 129
Bertoldi, F., & Draine, B. T. 1996, ApJ, 458, 222
Carpenter, J. M., Snell, R. L., & Schloerb, F. P. 1990, ApJ, 362, 147
Carpenter, J. M., Snell, R. L., Schloerb, F. P., & Skrutskie, M. F. 1993, ApJ, 407, 657
Elmegreen, B. G., & Lada, C. J. 1977, ApJ, 214, 725
Elmegreen, B. G., & Lada, C. J. 1978, ApJ, 219, 467
Elmegreen, B. G., & Moran, J. M. 1979, ApJ, 227, L93
Elmegreen, B. G. 1992, in Proceeding III Canary Island Winter School of Astrophysics, Star Formation in Stellar Systems, edited by G. Tenorio-Tagle, M. Prieto, and F. Sanchez (Cambridge University Press, Cambridge), p. 381
Elmegreen, B. G., Kimura, T., & Tosa, M. 1995, ApJ, 451, 675
Goldsmith, P. F., Young, J. S., & Langer, W. D. 1983, ApJS, 51, 203
Greene, T. P., Wilking, B. A., Andre, P., Young, E. T., & Lada, C. J. 1994, ApJ, 434, 614
Guetter, H. H., & Turner, D. G. 1996, AJ 113, 2116
Henning, T., Martin, K., Reimann, H.-G., Launhardt, R., Leisawitz, D., & Zinnecker, H. 1994, A&A, 288, 282
Hester, J. J., *et al.* 1996, AJ, 111, 2349
Hodapp, K.-W. 1994, ApJS, 94, 615
Israel, F. P. 1977, A&A, 60, 233
Kenyon, S. J., Hartmann, L. W., Strom, K. M., & Strom, S. E. 1990, AJ, 99, 869
Lefloch, B., & Lazareff, B. 1994, A&A, 289, 559 (LL94)

Leisawitz, D., Bash, F. N., & Thaddeus, P. 1989, ApJS, 70, 731
MacLaren, I., Richardson, K. M., & Wolfendale, A. W., 1988, ApJ, 333, 821
Mauersberger, R., Wilson, T. L., Mezger, P. G., Gaume, R., & Johnston, K. J. 1992, A&A, 256, 640
Megeath, S. T. 1994, in The Structure and Content of Molecular Clouds, edited by T. L. Wilson and K. J. Johnston (Springer, Berlin), p. 215
Megeath, S. T., Cox, P., Bronfman, L., & Roelfsema, P. R. 1996, A&A, 305, 296
Megeath, S. T., & Herter, T. L. 1997, in preparation
Oort, J. H., & Spitzer, L. 1955, ApJ, 121, 6
Panagia, N. 1973, AJ, 78, 929
Patel, N. A, Xie, T., & Goldsmith, P. F. 1993, ApJ, 413, 593
Patel, N. A, Goldsmith, P. F., Snell, R. L., Hezel, T., & Xie, T. 1995, ApJ, 447, 721
Reipurth, B. 1983, A&A, 117, 183
Sandford II, M. T., Whitaker, R. W., & Klein, R. I. 1982, ApJ, 260, 183
Serabyn, E., Güsten, R., & Mundy, L. 1993, ApJ, 404, 247
Snell, R. L., Dickman, R. L., & Huang, Y.-L. 1990, ApJ, 352, 139
Sugitani, K., Fukui, Y., & Ogura, K. 1991, ApJS, 77, 59
Sugitani, K., & Ogura, K. 1994, ApJS, 92, 163
Sugitani, K., Tamura, M., & Ogura, K. 1995, ApJ, 455, L39
Tielens, A. G. G. M., & Hollenbach, D. 1985, ApJ, 291, 722
Wainscoat, R. J., & Cowie, L. L. 1992, AJ, 103, 332
Xilouris, K. 1997, personal communication

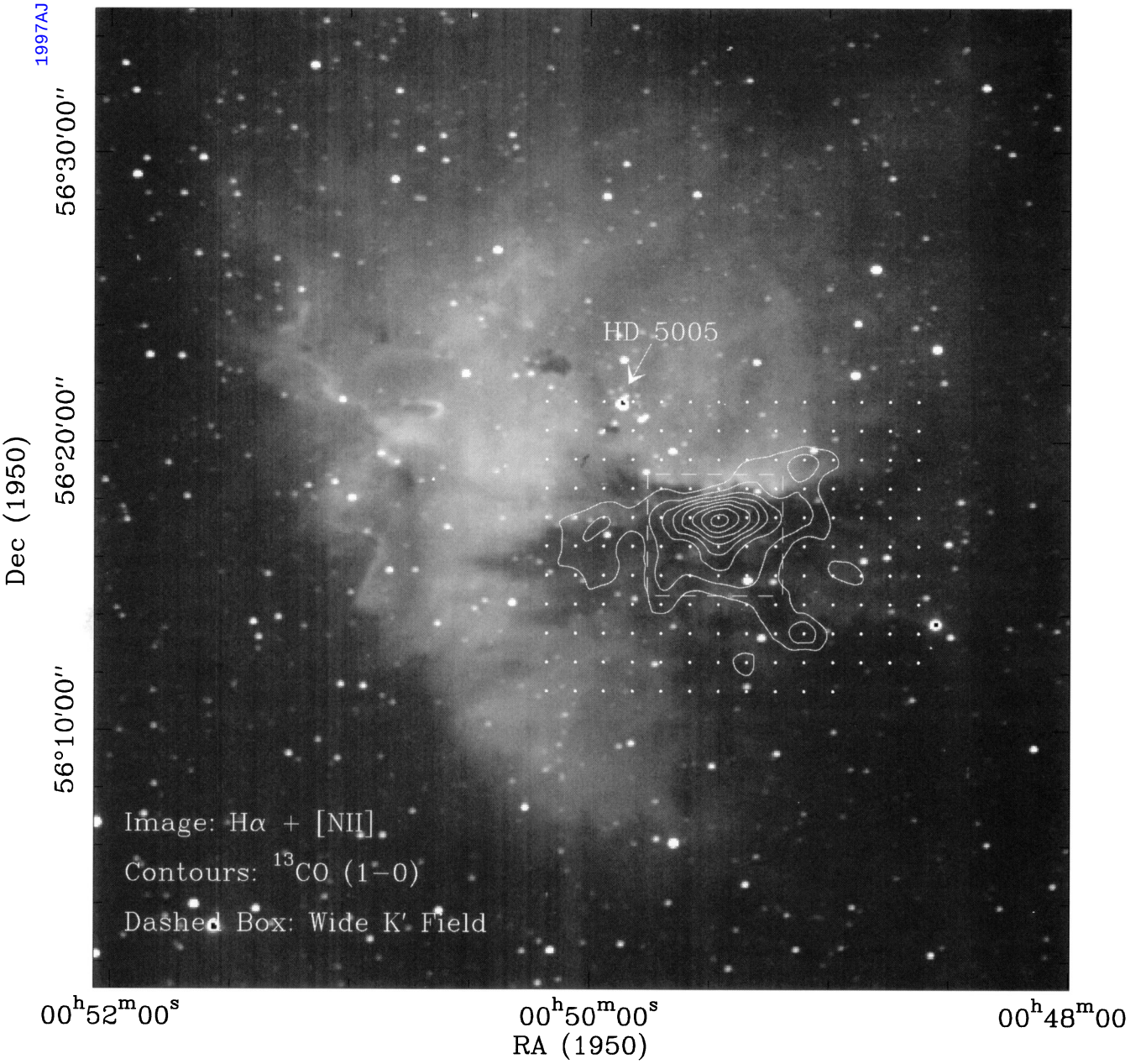

FIG. 1. A CCD image of NGC 281 in a narrowband filter centered on the Hα + [N II] lines (Xilouris 1997). The trapezium system HD 5005, which is marked with an arrow, is the primary source of ionizing UV radiation in the nebula. The contours show the velocity integrated ^{13}CO (1→0) emission mapped by Carpenter *et al.* (1990); the contours range from 3 to 19 by 2 K km s^{-1}. The dots mark the points observed in ^{13}CO (1→0). The dashed box outlines the region covered in our K'-band imaging. This figure shows that the molecular cloud is responsible for obscuring the southwestern quadrant of the roughly circular H II region (see radio map in Israel 1977). The ^{13}CO (1→0) map shows that the column density peaks near the H II region/molecular cloud interface. Elmegreen & Lada (1978) suggested that the peak was the result of molecular gas swept up by the expanding H II region.

S. T. Megeath and T. L. Wilson (see page 1107)

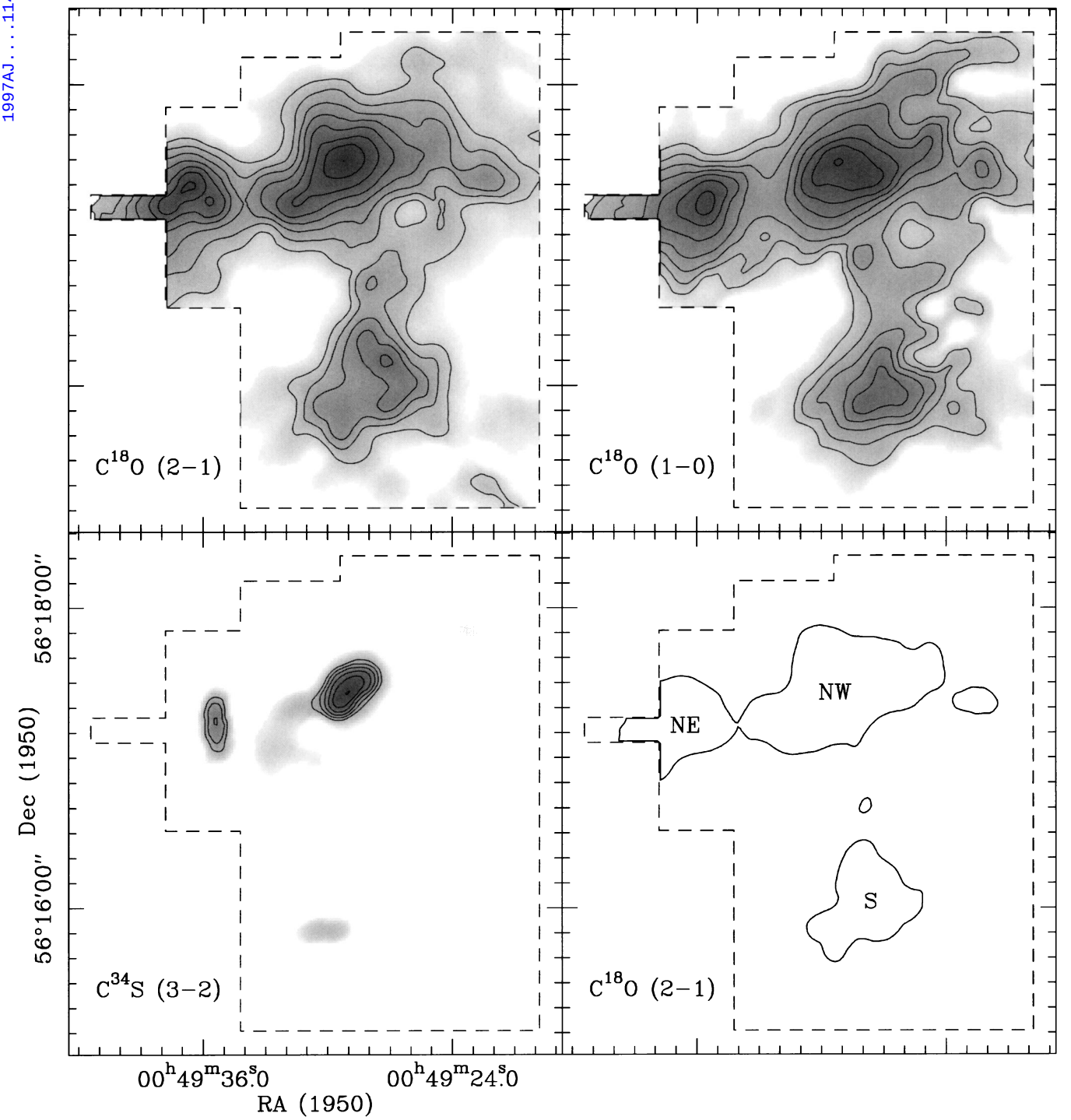

FIG. 2. Velocity integrated intensity line maps ($\int T_{MB} dv$) in the $C^{18}O$ (2→1), $C^{18}O$ (1→0), and $C^{34}S$ (3→2) transitions. The data were taken with the IRAM 30 meter telescope with FWHP beamwidths of 11″, 16″, and 22″ for the $C^{18}O$ (2→1), $C^{34}S$ (3→2), and $C^{18}O$ (1→0) lines, respectively. The map spacing is 10″. The contour levels are 5.24 to 17.47 by 1.75 K km s^{-1} for $C^{18}O$ (2→1), 3.39 to 6.78 by 0.68 K km s^{-1} for $C^{34}S$ (3→2), and 1.76 to 5.82 by 0.58 K km s^{-1} for $C^{18}O$ (1→0). The 5σ detection limits are 4.2, 2.1, and 1.5 K km s^{-1} for the $C^{18}O$ (2→1), $C^{34}S$ (3→2), and $C^{18}O$ (1→0) lines. The $C^{18}O$ (2→1) and $C^{18}O$ (1→0) maps show that the molecular gas is concentrated into three clumps, which we denote NW, NE, and S.

S. T. Megeath and T. L. Wilson (see page 1109)

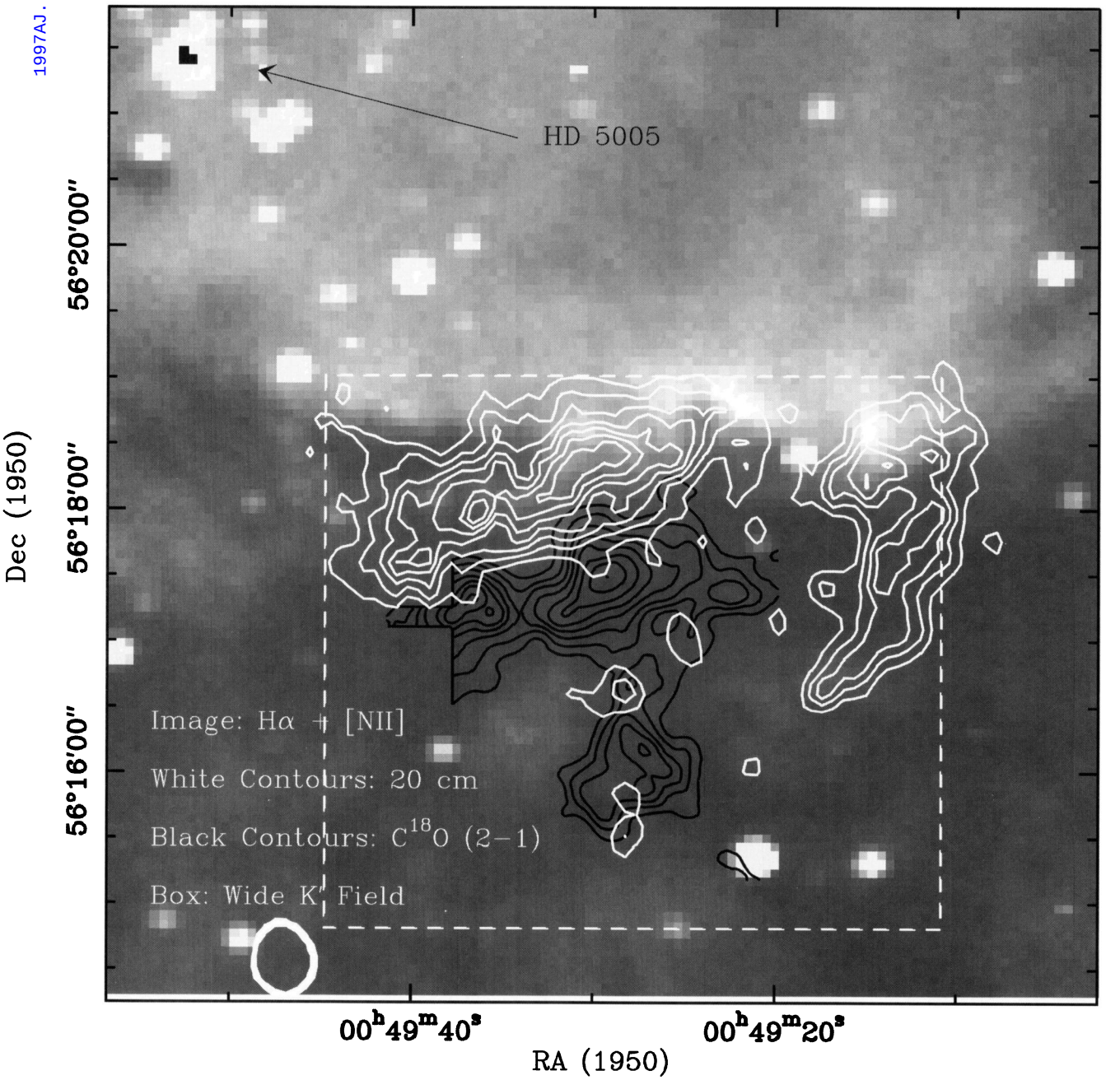

FIG. 5. A section of the Hα + [N II] image with the VLA 20 cm and IRAM 30 meter $C^{18}O$ (2→1) data superimposed. The dark contours are integrated $C^{18}O$ (2→1) emission with controus ranging from 5.24 to 17.47 by 1.75 K km s^{-1}. The continuous white contours show the 20 cm continuum with contours of 1.8 to 6 mJy/beam by 0.6 mJy/beam. The lowest 20 cm contour is at the 10σ level. This image illustrates the spatial relationship between the three molecular clumps detected in our $C^{18}O$ (2→1) maps, the ionized gas near the molecular clumps, and the hot OB stars ionizing the nebula. On the basis of this spatial relationship, we propose that all three clumps are exposed to the UV filed of HD 5005 and are photoevaporating. The bright 20 cm source in the lower left is thought to be a background extragalactic source.

S. T. Megeath and T. L. Wilson (see page 1111)

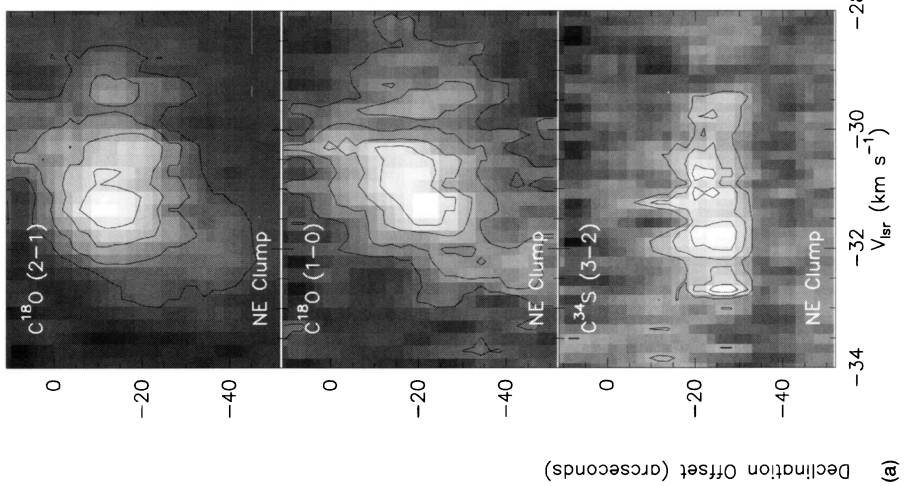

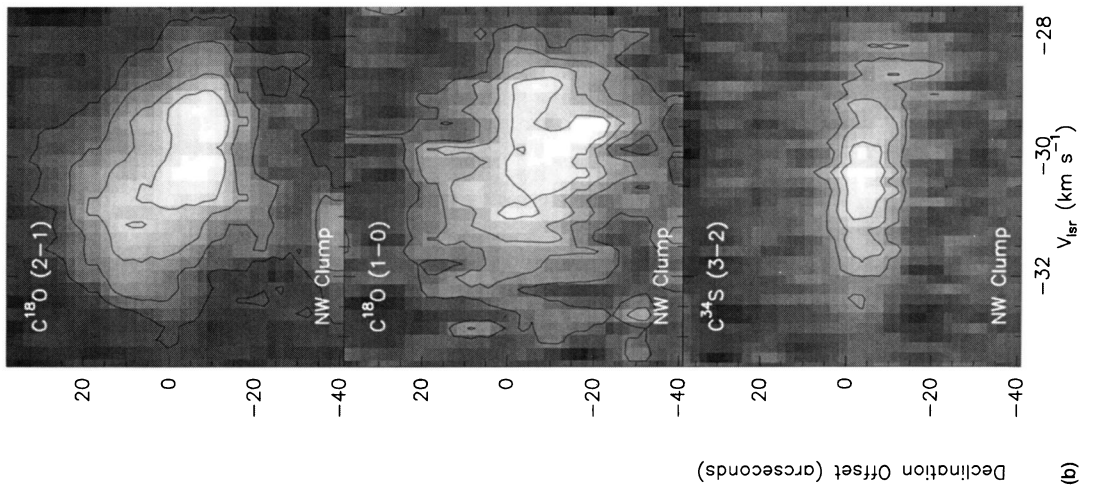

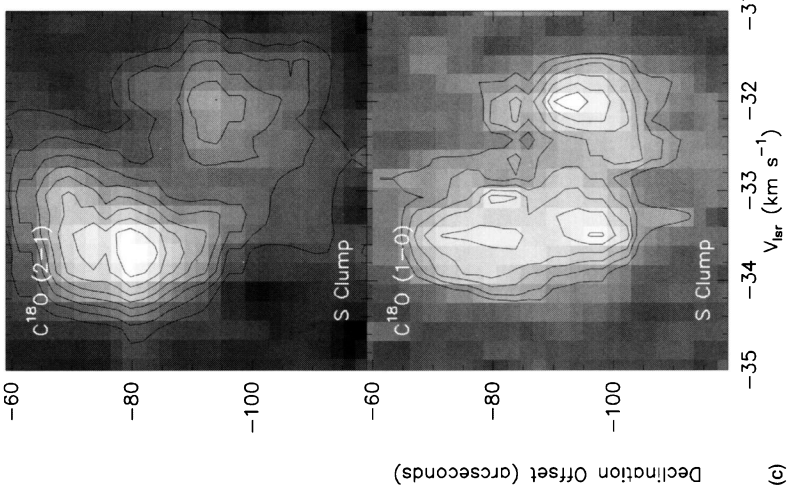

FIG. 6. (a) The position-velocity cut through the NE clump. The cut is shown in Fig. 3. The contour levels are 1.27 to 6.37 by 1.27 K, 0.43 to 2.15 by 0.43 K and 0.58 to 1.45 by 0.29 K for the $C^{18}O$ (1→0), $C^{18}O$ (2→1), and $C^{34}S$ (3→2), respectively. The slice is rotated 35° counterclockwise from the declination axis; the resulting beamsizes projected on the declination axis are 9″ $C^{18}O$ (2→1)), 18″ ($C^{18}O$ (1→0)), and 13″ ($C^{34}S$ (3→2)). (b) The position-velocity cut through the NW clump. The cut is given in Fig. 3. The contours are 1.03 to 5.14 by 1.03 K, 0.37 to 1.87 by 0.37 K, and 0.84 to 2.10 by 0.42 K for the $C^{18}O$ (2→1), $C^{18}O$ (1→0) and $C^{34}S$ (3→2), respectively. As in the case of the NE clumps, the slice is rotated 35° counterclockwise from the declination axis. (c) Position-velocity diagram for the *S* clump. The cut is shown in FIg. 3. The contour levels are 1.44 to 7.18 by 0.72 K, and 0.81 to 2.01 by 0.20 K for the $C^{18}O$ (2→1) and $C^{18}O$ (1→0), respectively. $C^{34}S$ (3→2) was not detected in the *S* clump. The slice is rotated 35° counterclockwise from the declination axs.

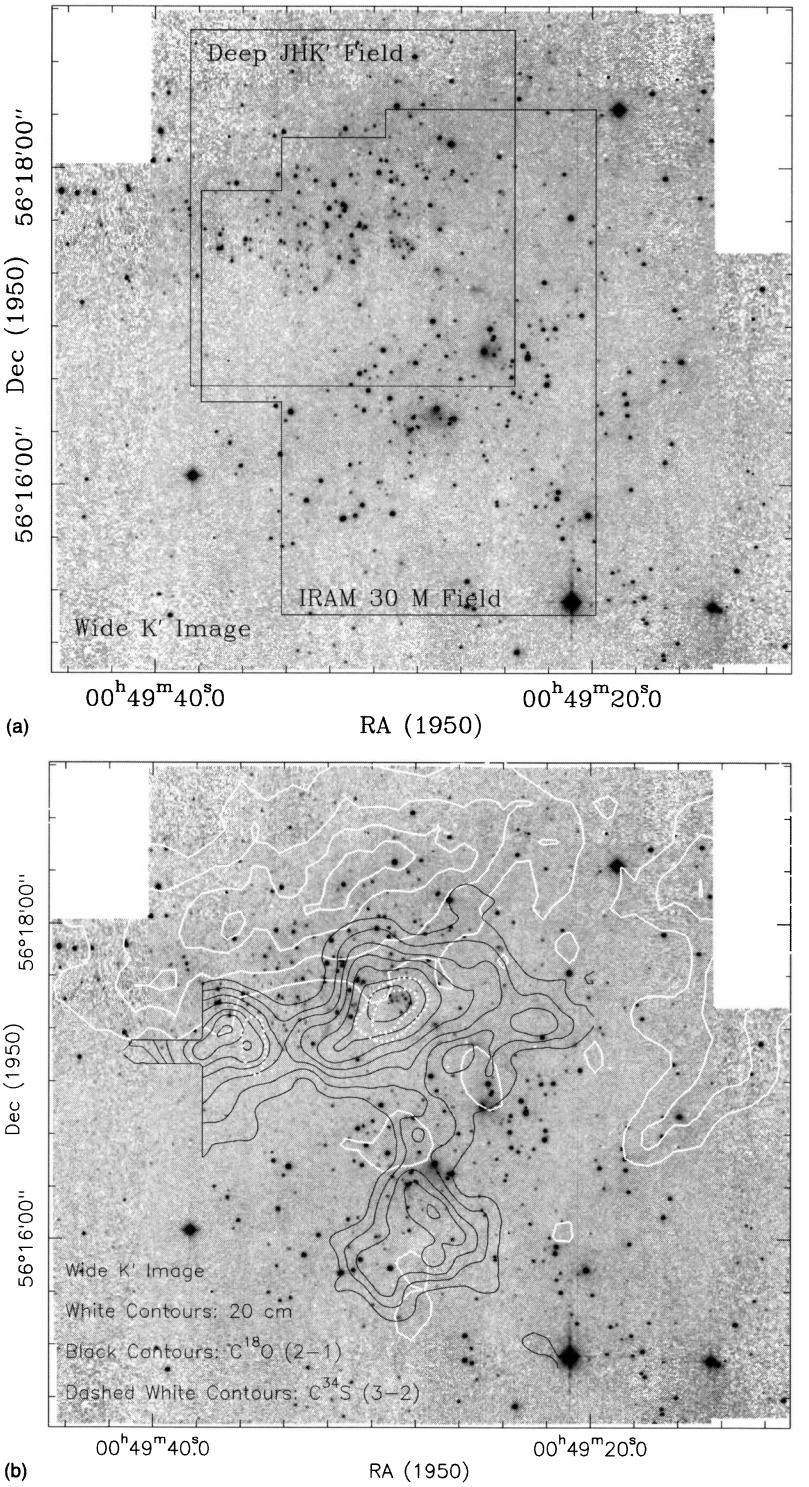

FIG. 7. (a) The K'-band mosaic of the NGC 281 West H II/molecular interface. We have outlined the regions covered in our deep JK' images of the northern sub-cluster and our IRAM 30 meter maps. The mosaic shows a cluster of primarily low-mass stars (Megeath 1994). Note that most of the stars in the image are associated with the molecular cloud; however, the four brightest stars in the field are foreground stars. The cluster is grouped into northern and southern sub-clusters. (b) The K'-band mosaic with the VLA and IRAM 30-meter maps overlayed. The dark contours are integrated $C^{18}O$ $(2\rightarrow1)$ emission with contours ranging from 5.24 to 17.47 by 1.75 K km s^{-1}. The dotted white contours toward the center of the two northernmost CO clumps show the $C^{34}S$ $(3\rightarrow2)$ emission. The contour levels are 3.4 and 5.1 K km s^{-1}. The continuous white contours show the 20 cm continuum with contours of 1.8 to 6 mJy/beam with a 1.2 mJy/beam spacing. The relative distribution of stars and clumps suggest that the cluster is divided into two sub-clusters. The northern sub-cluster appears to be forming from the NW and NE clumps, while the southern sub-cluster may have formed in part from the S clump.

S. T. Megeath and T. L. Wilson (see page 1115)

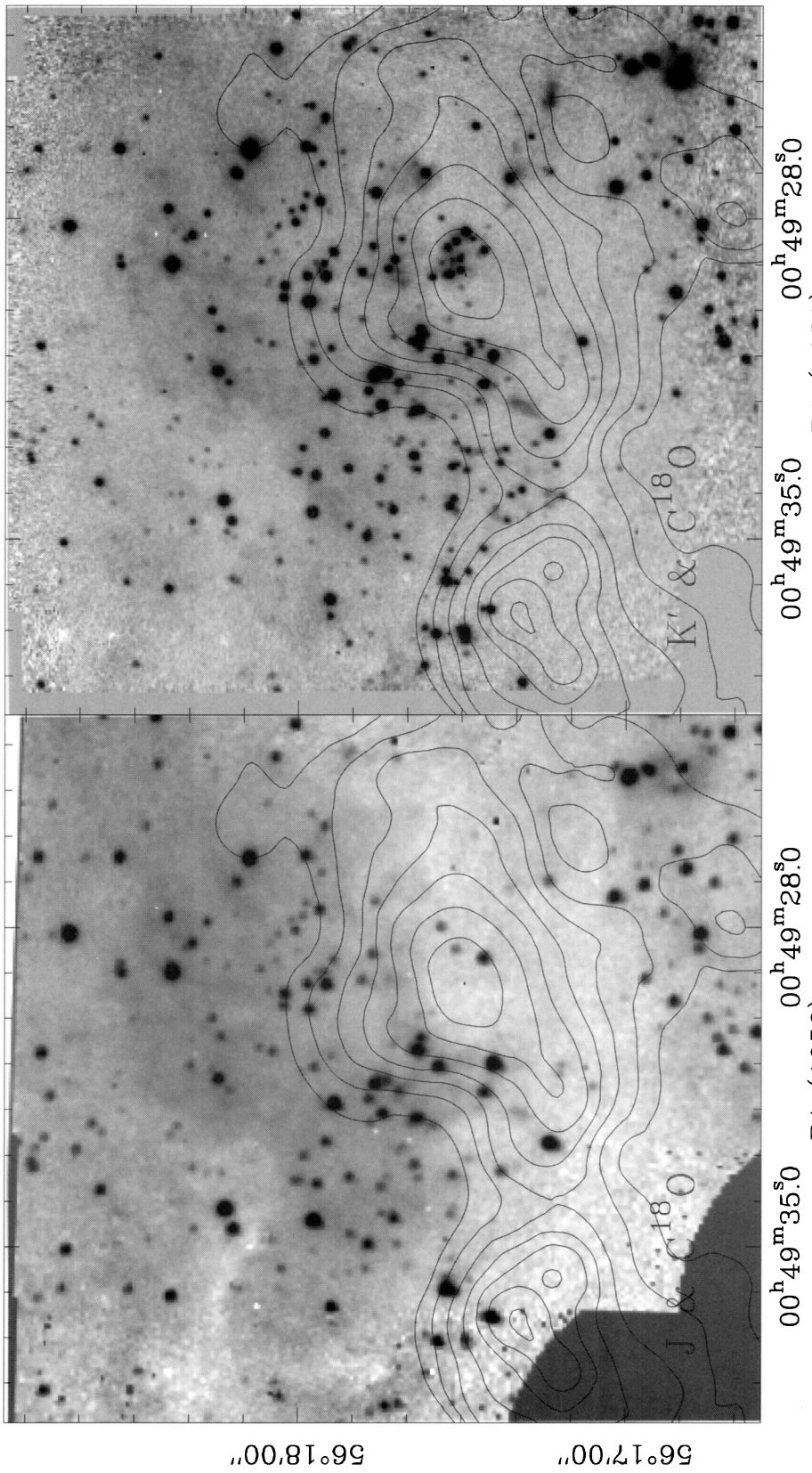

FIG. 9. **Right panel:** The deep K' ($m_K \leq 19$) image of the northern subcluster with the velocity integrated $C^{18}O$ (2→1) contour map overlayed. The $C^{18}O$ (2→1) contours range from 5.24 to 17.47 by 1.75 K km s^{-1}. **Left panel:** J-band image of the northern subcluster. The K' image is 80% complete to 18.5 mag in non-confused areas of the image, and 40% complete to this magnitude in regions of high stellar density. The most striking feature in these images is that the stars coincident with the NW and NE $C^{18}O$ (2→1) clumps are concentrated in the northern halves of the two clumps.

S. T. Megeath and T. L. Wilson (see page 1116)